Section 1. No dihedral angle offset

A. Hollow cube corner

No polarization effects

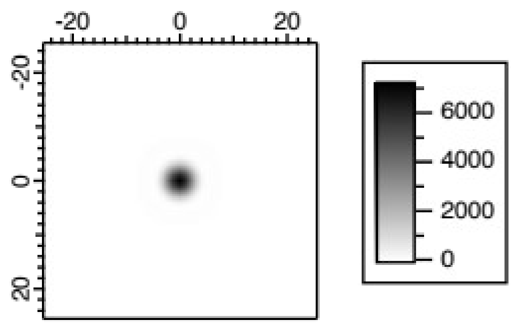

Figure 1.a

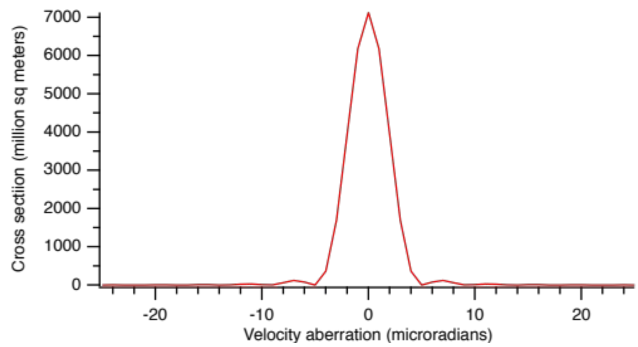

Figure 1.b

Figure 1. Hollow cube corner, dihedral angle offset = 0 arcsec, maximum cross section = 7124 million sq. m, wavefront deviation $\gamma = 0$. Part (a) is the far field cross section matrix. Part (b) is the cross section along the X axis. This is a classic Airy disc. For a 5 inch (d = .127m) retroreflector at λ = 532 nanometers, the first dark ring of the pattern using Equation (1) is at $\vartheta = 1.22\frac{\lambda}{d} = 1.22\frac{532\,nm}{.127\,m} = 5.002$ microradians

Using Equation (2) the cross section C at the center of the pattern is $C = 4\pi\left(\frac{A}{\lambda}\right)^2$ = 7124.9 million sq m

B. Solid coated cube corner

For a perfect metal, there are no polarization effects. For a real metal the effects of polarization are usually small. This calculation is for a perfect metal.

no dihedral angle offset
no polarization effects

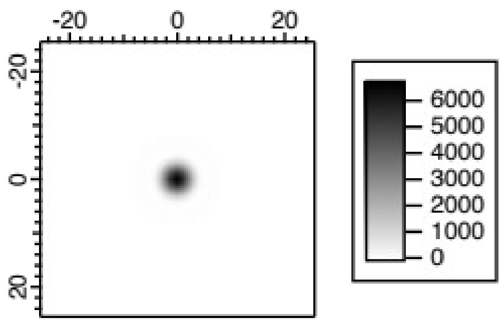

Figure 2.a

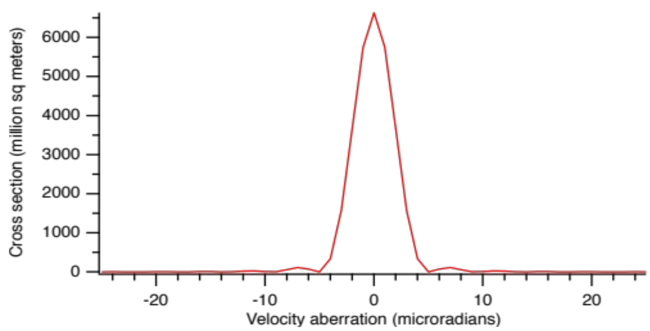

Figure 2.b

Figure 2. Solid coated cube corner, dihedral angle offset = 0, maximum cross section = 6633 million sq.m. There is a reduction of a factor of .93 compared to a hollow cube corner (Figure 1) due to reflection losses on entering and leaving the front face. The shape of the pattern is close to that of a classic Airy disc.

C. Solid uncoated cube corner

The polarization is given by a vector (X,Y) with complex components:

Polarization 1 = (X,Y) = $(1 + 0.0\,i,\ 0.0 + i)/\sqrt{2}$

No dihedral angle offset

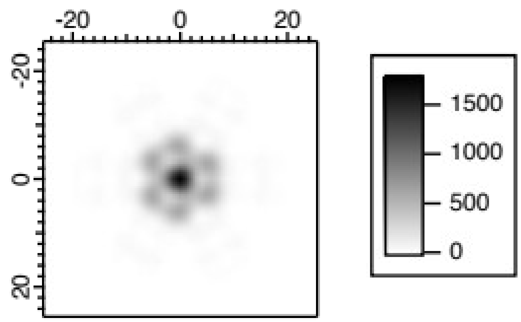

Figure 3.a

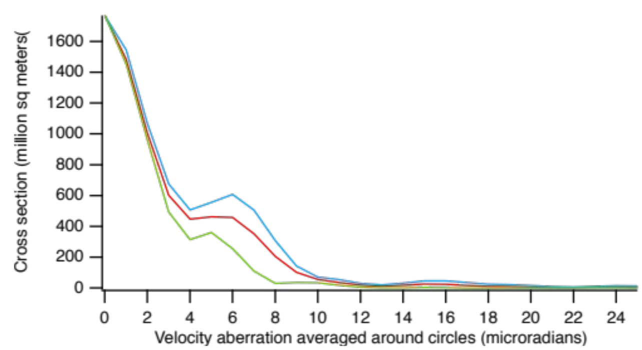

Figure 3.b

Figure 3. Solid uncoated cube corner, dihedral angle offset = 0, circular polarization 1, maximum cross section = 1768 million sq. m. Since the pattern has 6 lobes, the average cross section as a function of the distance from the center is plotted. The average (red), maximum (blue) and minimum (green) around a circle in the far field are plotted vs the magnitude of the velocity aberration.

Note that circular polarization does not give a perfectly circular pattern. The asymmetry is very small. The diffraction pattern looks about the same for all polarization states. When a dihedral angle offset is added the patterns are very different for each polarization state.

This is not a classic Airy disc. The physical dimensions of the retroreflector are the same as the hollow and solid coated cases. But, the diffraction pattern is completely different because of the polarization effects caused by total internal reflection.

There is a loss of a factor of 3.75 in the maximum cross section compared to a solid coated cube corner (Figure 2) due to phase changes on total internal reflection. For each order of reflection, the phase change is different. There is never a flat wavefront to give high cross section. On the Apollo Lunar retroreflector arrays the coating was eliminated because it absorbs solar radiation and causes thermal gradients in the fused silica when sunlit.

Dihedral Angle Offsets

The following cases have a single dihedral angle offset in the vertical axis as shown in fig 6.a from (Arnold,1979). This creates 2 spots horizontally.

2.6 Input and Output Apertures

As shown in Section 2.3, the retroreflected ray leaves along a line on the opposite side of the vertex from the incident ray. Figure 6a shows the retroreflector from the direction of the incident beam; a ray incident at point A will be retroreflected from point B, which is an equal distance on the other side of the vertex O. Similarly, point C moves to point D. For any shaped retroreflector face, the shape of the retroreflected beam can be constructed by moving each point on the outline of the face an equal distance on the other side of the vertex. Figure 6b shows the result for a triangular retroreflector at normal incidence. The solid line, the shape of the retroreflector face, is called the input aperture, and the dotted line, giving the outline of the retroreflected beam, is the output aperture. The overlap of the two figures is the active reflecting area. Any ray that is incident outside the overlap region will not be retroreflected, since the symmetry of the incident and the reflected rays would require that the last reflection occur at a point outside the cube corner.

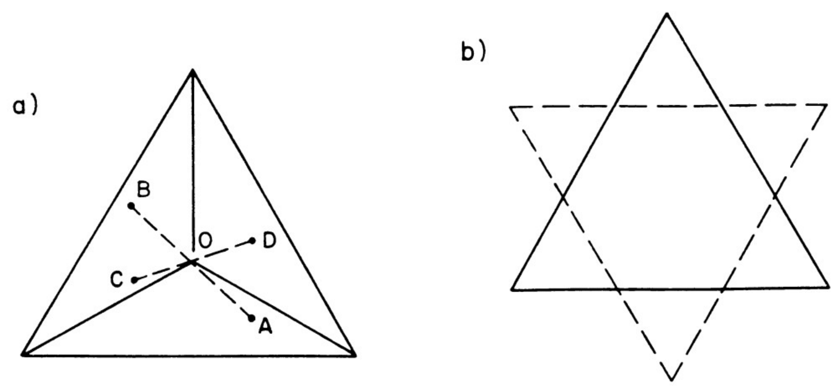

Figure 6. a) Method of constructing the output aperture; b) triangular input and output apertures.

Single Dihedral angle offset = 0.5 arcsec

A. Hollow cube corner

There are no polarization effects

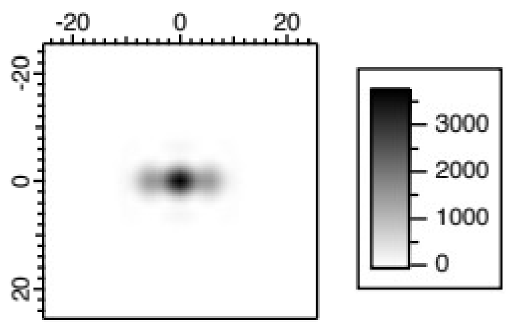

Figure 4.a

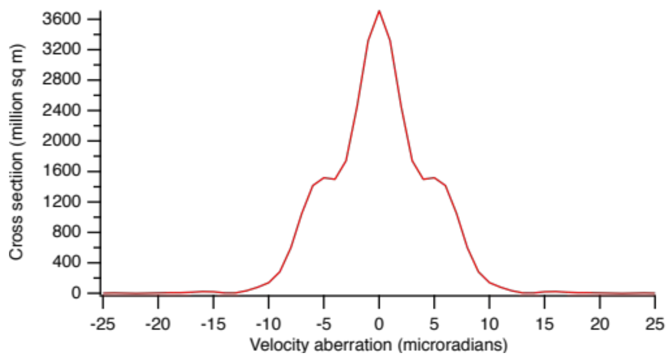

Figure 4.b

Figure 4. Hollow cube corner, dihedral offset = 0.5 arcsec, maximum cross section = 3713 million sq.m, wavefront deviation γ =3.96 microradians. The pattern does not show a peak at 3.96 microradians. This is because the deviation of the wavefront is comparable to the natural width due to diffraction.

B. Solid coated cube corner

Dihedral angle offset .5 arcsec
There are no polarization effects

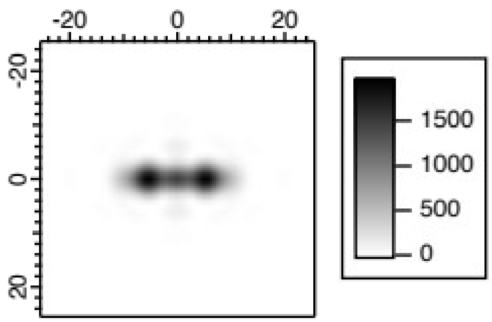

Figure 5.a

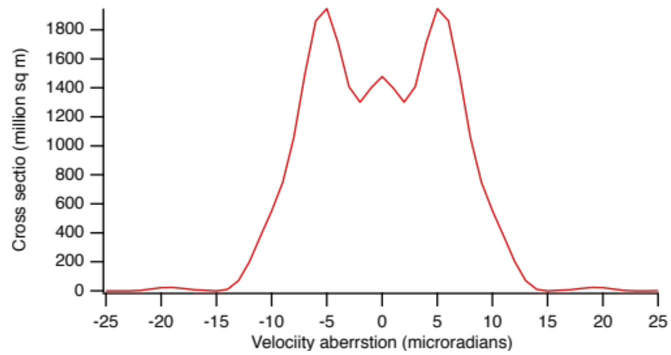

Figure 5.b

Figure 5. Solid coated cube corner, dihedral offset = 0.5 arcsec, maximum cross section = 1946 million sq.m, wavefront deviation γ = 5.78 microradians. The deviation of the wavefront is larger because of the index of refraction n = 1.461. There is a peak a little past 5 microradians because the wavefront deviation is larger than the natural width due to diffraction.

C. Solid uncoated cube corner

This section includes two cases for a five inch cube and one case for a four inch cube. The four inch case is included because the NGLR project uses a four inch uncoated cube corner.

a. circular polarization 1, five inch cube

Five inch uncoated retroreflector
Polarization 1 = (X,Y) = (1 + 0.0 i, 0.0 + i)/$\sqrt{2}$

Dihedral angle offset .5 arcsec

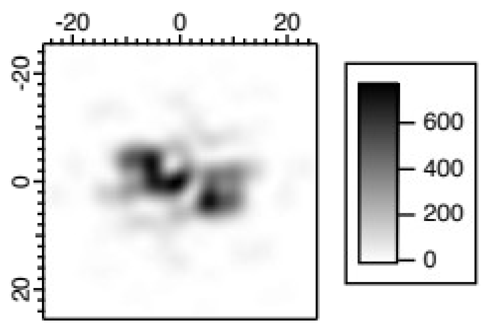

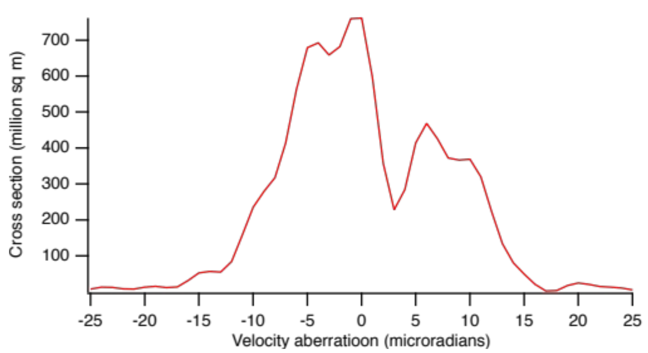

Figure 6.a Figure 6.b

Maximum cross section 761 million sq. m.

b. circular polarization 2, five inch cube

Five inch uncoated retroreflector
Polarization 2 = (X,Y) = (1 + 0.0 i,   0.0 - i)/$\sqrt{2}$

Dihedral angle offset .5 arcsec

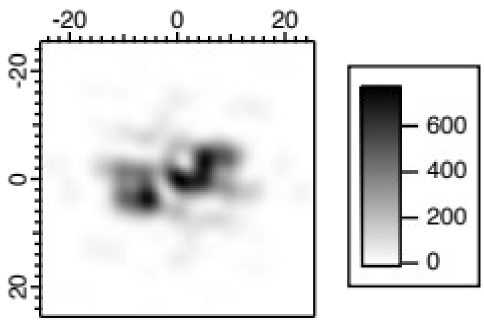

Figure 6.c

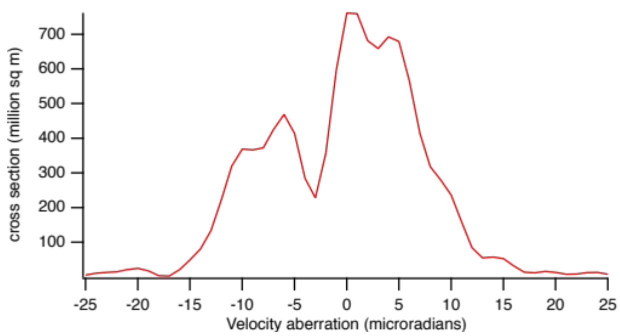

Figure 6.d

Maximum cross section 761 million sq. m.

c. circular polarization 1, four inch cube

Four inch uncoated retroreflector.
Polarization 1 = (X,Y) = (1 + 0.0 i, 0.0 + i)/$\sqrt{2}$

Dihedral angle offset .5 arcsec

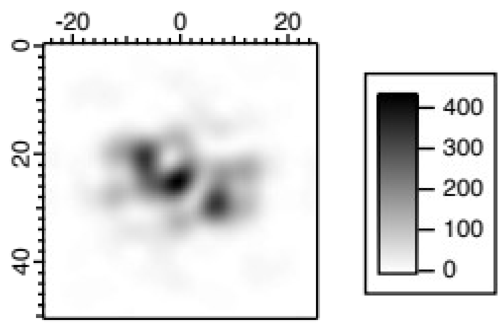

Figure 6.e

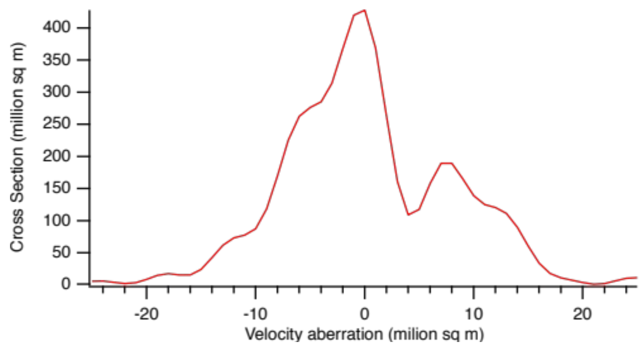

Figure 6.f

Maximum cross section 427 million sq. m.

Compare polarization 1 and polarization 2 for a five inch uncoated cube (Figs 6.b and 6.d)

Dihedral angle offset .5 arcsec

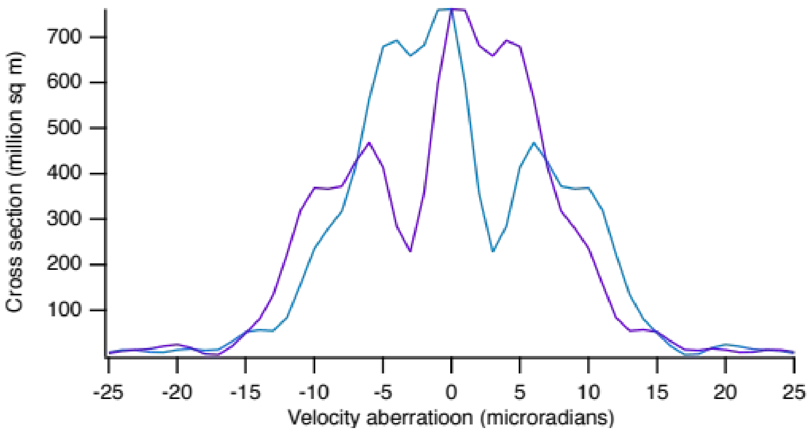

Figure 6.g. Solid 5 inch uncoated cube. Compare Fig, 6.b (polarization 1, blue) with Fig. 6.d (polarization 2, purple). Dihedral angle offset .5 arcsec. The patterns are mirror images of each other.

Figure 6. Solid uncoated cube corner, dihedral angle offset = 0.5 arcsec, wavefront deviation γ = 5.78 microradians, circular polarizations 1and 2. Maximum cross section for five inch cube = 761 million sq. m. Maximum cross section for four inch cube= 427 million sq. m.

The cross section ratio between five inch (761) and four inch (427) cubes = 1.78. The diameter ratio is 1.25. The area ratio is 1.5625. The four inch cube loses some cross section compared to a five inch cube because the diffraction spreading is greater.

Analysis

All the patterns in Figure 6 are completely different from Figure 5. The only physical difference is that the coating has been removed for Figure 6. The complicated structure in Figure 6 is due to polarization, and the interaction between the dihedral angle offset and the polarization caused by total internal reflection. The two spots caused by the dihedral angle offset overlap for the uncoated case because of the additional spreading of the spots due to polarization effects. In contrast to hollow and solid coated retroreflectors, the shape of the diffraction pattern of an uncoated retroreflector is a function of the transmitted polarization. For example, the slope of the bright spots is different in Figures 6.a and 6.c. In principle, changing the transmitted polarization might provide a way to optimize the cross section for the particular observing geometry.

Compare a five inch (red) cube with a four inch (green) uncoated cube.

Dihedral angle offset .5 arcsec
Polarization 1

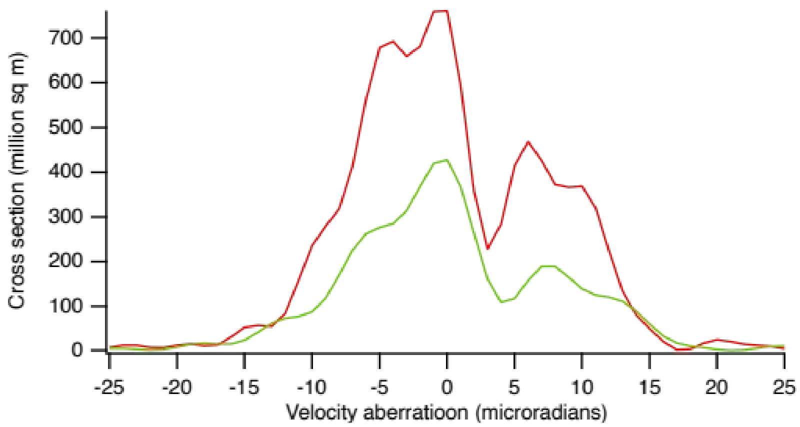

Figure 7.a. Compare Figure 6.b (red, five inch) with Figure 6.f (Green, four inch), dihedral angle offset .5 arcsec.

The maximum cross section (761 vs 427) is much lower for the four inch retroreflector because of two factors. The reflecting area is lower and the size of the spots is larger due to diffraction.

Compare a five inch (red) cube with a four inch (green) uncoated cube.

Dihedral angle offset .5 arcsec
Polarization 1

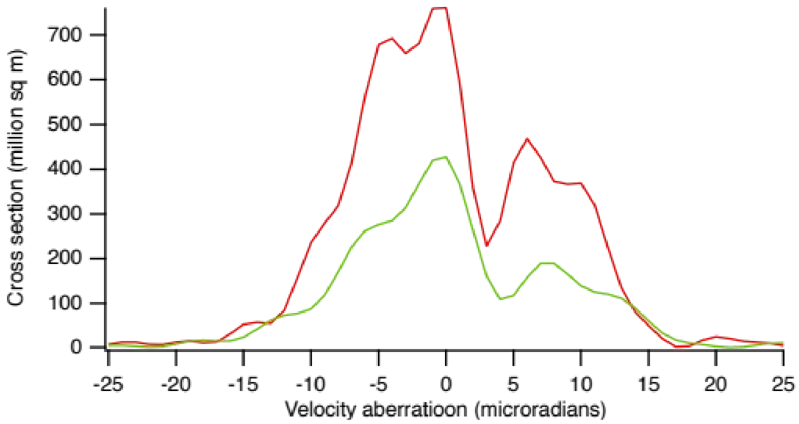

Figure 7.a. Compare Figure 6.b (red, five inch) with Figure 6.f (Green, four inch), dihedral angle offset .5 arcsec.

The maximum cross section (761 vs 427) is much lower for the four inch retroreflector because of two factors. The reflecting area is lower and the size of the spots is larger due to diffraction.

Compare hollow (red), solid coated (green), and solid uncoated retroreflectors (blue and purple).

Five inch cube.
Dihedral angle offset .5 arcsec
Polarizations 1 and 2 for uncoated cube

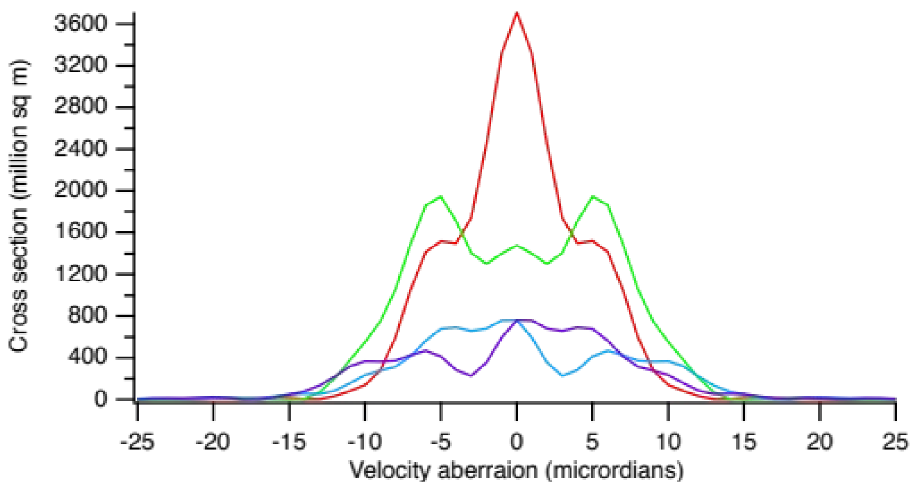

Figure 7.b All curves are for a five inch retroreflector. Compare Fig. 4.b (hollow, red), Fig. 5.b (solid coated, green), Fig. 6.b (solid uncoated, blue, polarization 1), and Fig. 6.d (solid uncoated, purple, polarization 2).

See also Fig. 6.g for details of the blue and purple curves. The uncoated cube has the lowest cross section because of polarization effects.

Comparison with NGLR simulations

A calculation has been done for the case of a four inch uncoated cube corner with linear polarization and a .5 arcsecond dihedral angle offset. It is not presented here because it was done under contract to INFN/LNF.

INFN/LNF has commercial software for computing the diffraction pattern of a retroreflector. For the sake of program validation, comparisons were done for a four inch uncoated cube corner with horizontal polarization and dihedral angle offsets in the three axes of (0, 0, 0), (.1, .1, .1), and (.5, .1, .1) arcseconds. The comparisons were satisfactory.

The comparisons done with the NGLR project were part of the motivation for this paper and the primary reason for the particular cases selected.

Section 3. Single Dihedral angle offset = 1.0 arcsec

A. Hollow cube corner

Dihedral angle offset 1.0 arcsec
No polarization effects

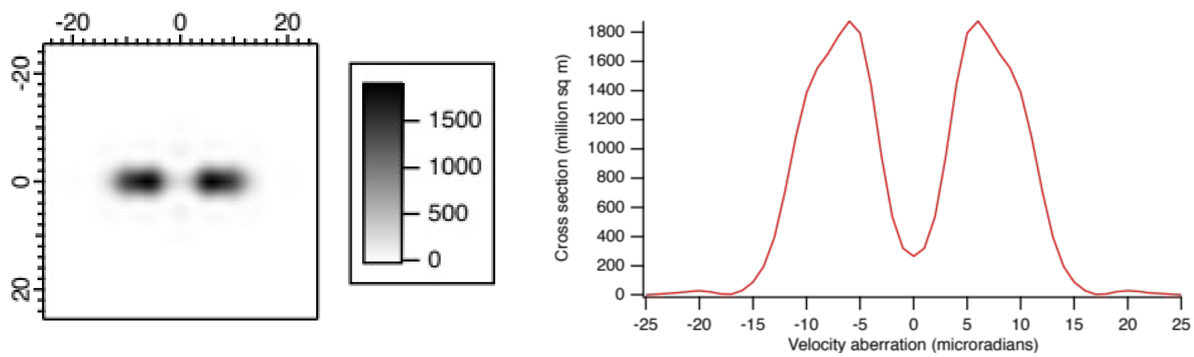

Figure 8.a Figure 8.b

Figure 8. Hollow cube corner, dihedral angle offset = 1.0 arcsec, maximum cross section= 1876 million sq. m, deviation of the wavefront γ = 7.92 microradians. The two spots are essentially separate from each other because the deviation of the wavefront by the dihedral angle offset is larger than the diffraction spreading.

B. Solid coated cube corner

Dihedral angle offset 1.0 arcsec
No polarization effects

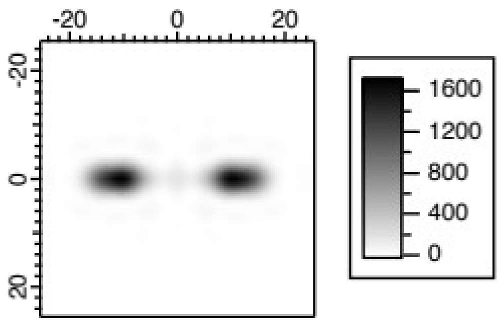

Figure 9.a

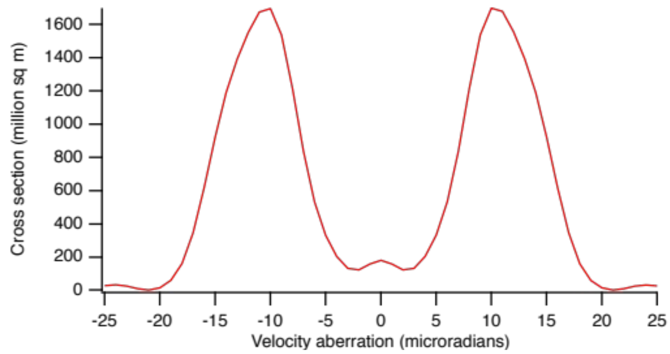

Figure 9.b

Figure 9. Solid coated cube corner, dihedral angle offset = 1.0 arcsec,
maximum cross section = 1697 million sq. m, wavefront deviation γ = 11.57 microradians.
The solid cube has a larger separation of the spots than the hollow cube because of the index of refraction = 1.461.

C. Solid uncoated cube corner

a. Polarization 1

Polarization 1 = (X,Y) = (1 + 0.0 i, 0.0 + i)/$\sqrt{2}$
Dihedral angle offset 1.0 arcsec
Uncoated cube

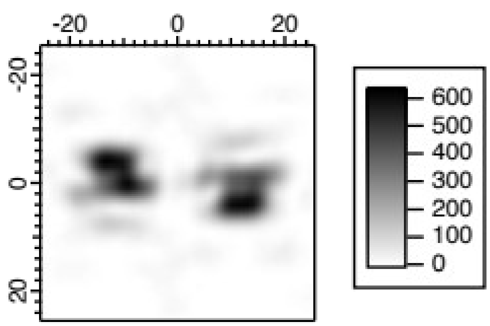

Figure 10.a

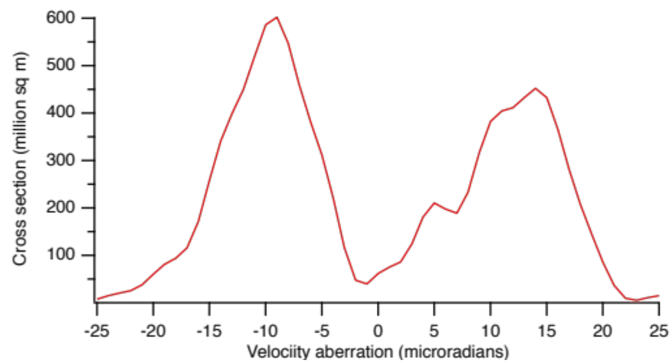

Figure 10.b

Figure 10. Solid uncoated cube corner, dihedral angle offset = 1 arcsec,
maximum cross section = 627 million sq. m, wavefront deviation γ = 11.57 microradians.
Circular Polarization 1 = (X,Y) = (.707106781 + i 0.0, 0.0 + i 0.707106781).

Polarization effects create complicated patterns. The two spots are separated from each other because the wavefront deviation due to the dihedral angle offset is larger than the diffraction spreading.

b. Polarization 2

Polarization 2 = (X,Y) = (1 + 0.0 i,   0.0 - i)/$\sqrt{2}$
Dihedral angle offset 1.0 arcsec
Uncoated cube

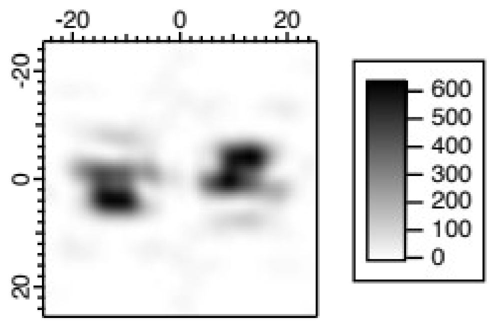

Figure 11.a

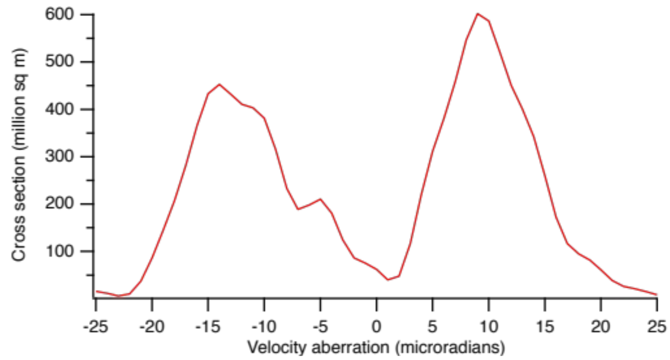

Figure 11.b

Figure 11. Solid uncoated cube corner, dihedral angle offset = 1 arcsec,
maximum cross section = 626 million sq. m, wavefront deviation γ = 11.57 microradians.

Compare polarizations 1 and 2.

Dihedral angle offset 1.0 arcsec
Uncoated cube

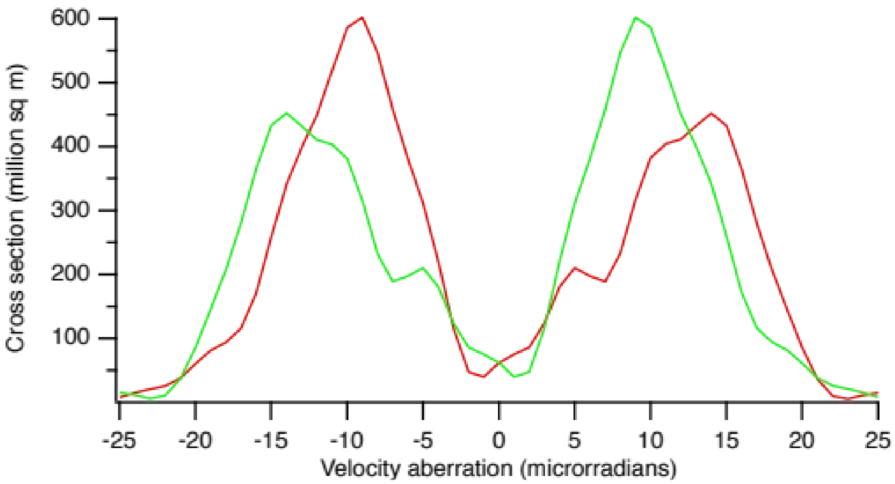

Figure 12. Compare Figures 10.b and 11.b (circular polarization)

Red = Polarization 1

(X,Y) = (1 + 0.0 i, 0.0 + i)/$\sqrt{2}$

Green = Polarization 2

(X,Y) = (1 + 0.0 i, 0.0 - i)/$\sqrt{2}$

The patterns for polarizations 1 and 2 are mirror images of each other.

Compare hollow (red), solid coated (green), and solid uncoated retroreflectors (blue)

Dihedral angle offset 1.0 arcsec
Circular Polarization 1 for uncoated

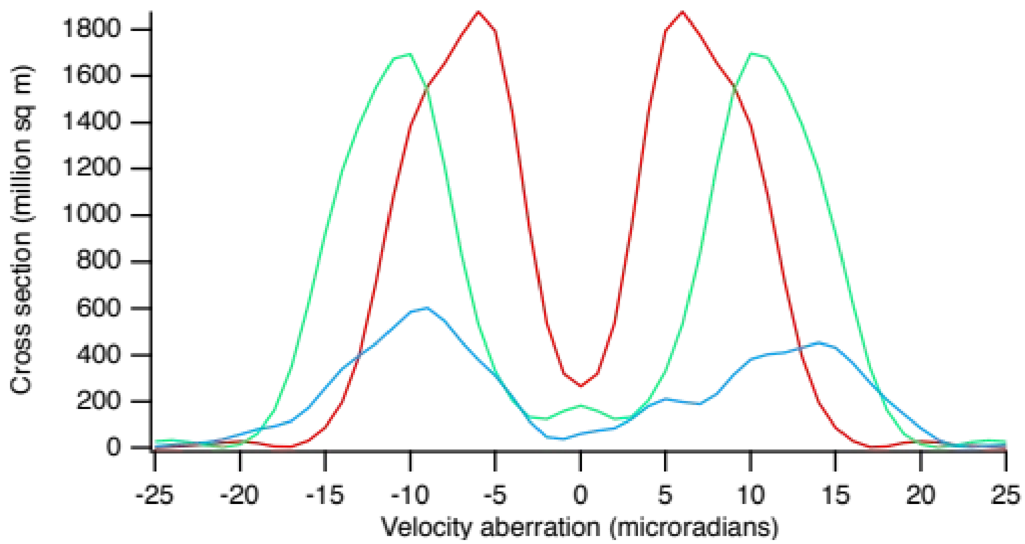

Figure 13. Compare Figure 8.b (red = hollow), Figure 9.b (Green = solid coated), and Figure 10.b (Blue = solid uncoated with circular Polarization 1).

The cross section of an uncoated retroreflector is much lower than for a coated or hollow retroreflector because of polarization effects.

c. Horizontal polarization

Horizontal Polarization = (X,Y) = (1.0 + i 0.0, 0.0 + i 0.0).
Dihedral angle offset 1.0 arcsec
Uncoated cube

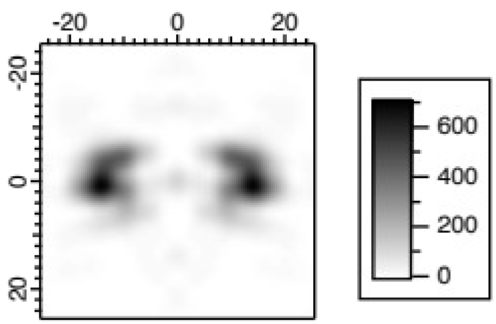

Figure 14.a

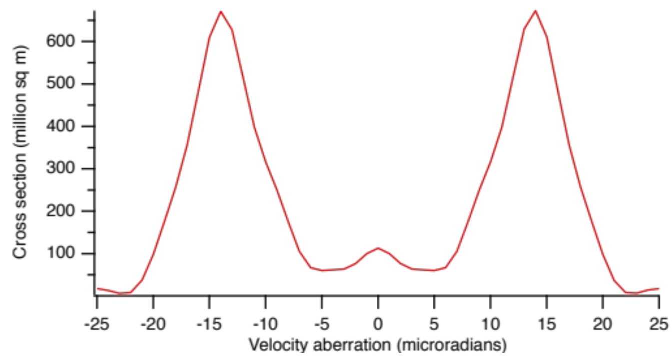

Figure 14.b

Figure 14. Solid uncoated cube corner, horizontal polarization, dihedral angle offset = 1.0 arcsec, maximum cross section = 700 million sq. m, wavefront deviation γ = 11.57 microradians,

The two spots have complicated shapes because of polarization effects. They are separated because of the large wavefront deviation due to the dihedral angle offset.

d. Vertical polarization

Vertical Polarization = (X,Y) = (0.0 + i 0.0, 1.0 + i 0.0)
Dihedral angle offset 1.0 arcsec
Uncoated cube
.

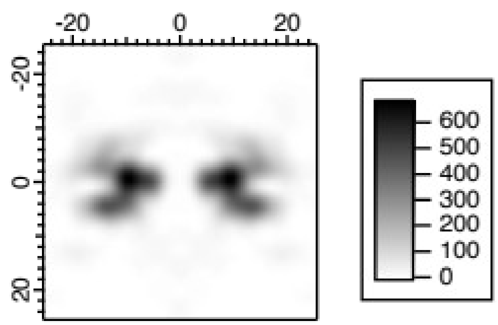

Figure 15.a

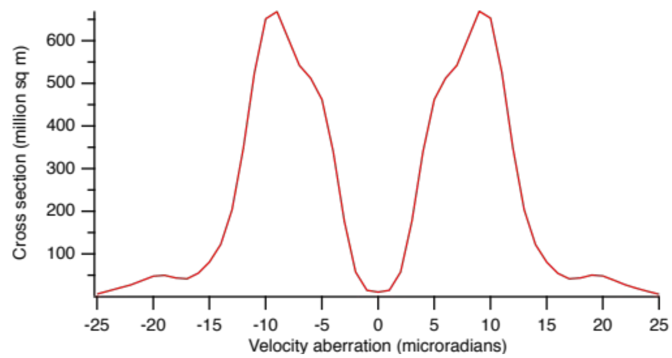

Figure 15.b

Figure 15. Solid uncoated cube corner, vertical polarization, dihedral angle offset = 1.0 arcsec, maximum crosss section = 676 million sq. m, γ = 11.57 microradians,

Compare horizontal (red) and vertical polarization (green).

Dihedral angle offset 1.0 arcsec
Uncoated cube

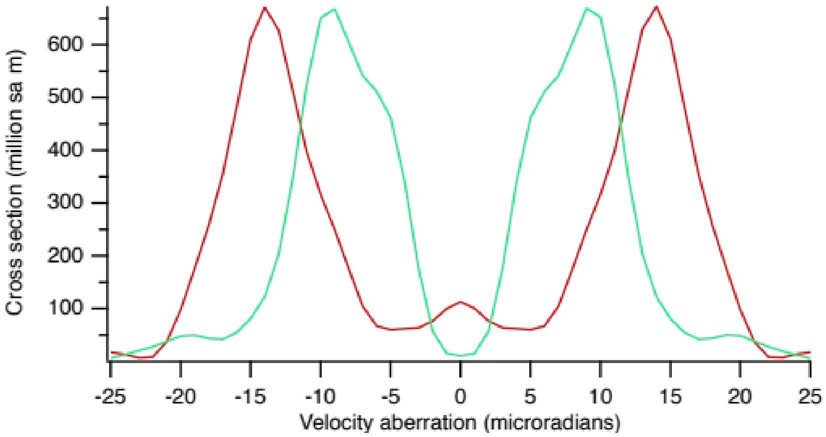

Figure 16. Solid uncoated retroreflector. Compare Figures 14.b (horizontal polarization, red}and 15.b (vertical polarization, green), dihedral angle offset 1.0 arcsec.
Red = Horizontal Polarization
(X,Y) = (1.0 + i 0.0, 0.0 + i 0.0)
Green = Vertical Polarization
(X,Y) = (0.0 + i 0.0, 1.0 + i 0.0)

The patterns are not mirror image.

4. Apollo Lunar retroreflector arrays

A. Cross section of the Apollo arrays.

The Apollo arrays use an array of 1.5 inch solid uncoated cube corners with no dihedral angle offset. The far field cross section matrix of a single cube corner is shown in Figure 17 and Table 2. The cross section of the whole array can be obtained by multiplying the cross section of a single cube corner by the number of cube corners (100 Apollo 11 and 14, or 300 Apollo 15).

Cross section of a single 1.5 inch Apollo cube corner
No dihedral angle offset
Uncoated cube

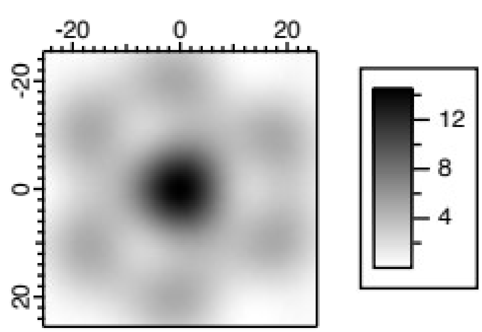

Figure 17.a

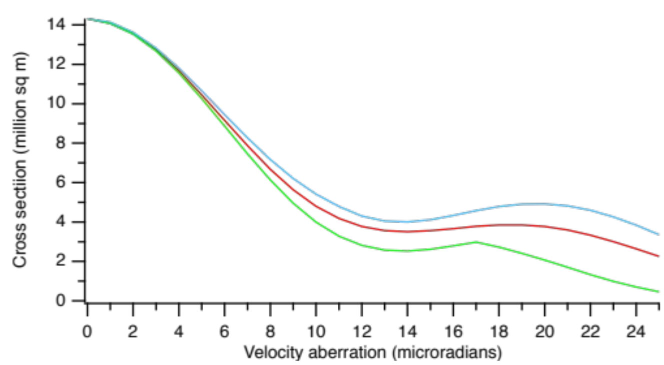

Figure 17.b

Figure 17. Cross section of a single Apollo cube corner. Part (a) is the cross section matrix. The axes are in microradians. The cross section is in million sq. m. Part (b) is the average (red), minimum (green), and maximum (blue) around circles in the far field.

Data used to plot figure 17.b

Microradians	Minimum	Average	Maximum	Max - Min
0.0	14.3237209	14.3237209	14.3237209	0.0000000
1.0	14.0688198	14.0953440	14.1454364	0.0766166
2.0	13.5297012	13.5704795	13.6315885	0.1018873
3.0	12.6721243	12.7439181	12.8317217	0.1595974
4.0	11.5650177	11.6795890	11.8144993	0.2494816
5.0	10.2597158	10.4522532	10.6600394	0.4003237
6.0	8.8704135	9.1558238	9.4513827	0.5809692
7.0	7.4558435	7.8695391	8.2661213	0.8102778
8.0	6.1294098	6.6765294	7.1704960	1.0410861
9.0	4.9562915	5.6389804	6.2074209	1.2511294
10.0	3.9973639	4.7997834	5.4178154	1.4204516
11.0	3.2826506	4.1793567	4.7838047	1.5011542
12.0	2.8166477	3.7766124	4.3093715	1.4927237
13.0	2.5799818	3.5671232	4.0492513	1.4692695
14.0	2.5335662	3.5112358	4.0130228	1.4794566
15.0	2.6246298	3.5650585	4.1213316	1.4967018
17.0	2.9822538	3.7835404	4.5812953	1.5990414
16.0	2.7937884	3.6716342	4.3328855	1.5390971
18.0	2.7256950	3.8554016	4.7877164	2.0620214
19.0	2.4163737	3.8577372	4.9093258	2.4929521
20.0	2.0696659	3.7735090	4.9191074	2.8494414
21.0	1.7023294	3.5976760	4.8172309	3.1149015
22.0	1.3359878	3.3371898	4.5966550	3.2606672
23.0	0.9943455	3.0097696	4.2662029	3.2718574
24.0	0.6992341	2.6405997	3.8391553	3.1399212
25.0	0.4672688	2.2554576	3.3540912	2.8868224

Table 2. Cross section (million sq. m) of an Apollo cube corner vs the magnitude of the velocity aberration (microradians). Columns 2 - 5 are the minimum, average, maximum, and max-min around circles of increasing diameter in the far field.

A calculation of the off axis cross section is given in the paper (Arnold, 2005).

Cross section vs velocity aberration for a 100 cube Apollo array

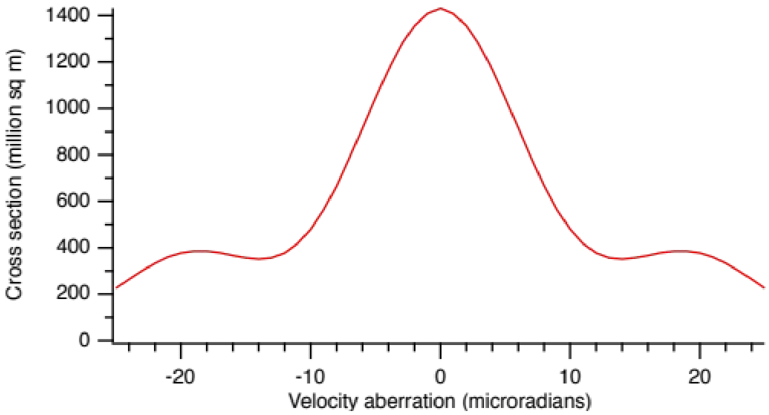

Figure 18. Average cross section in million sq. m vs the magnitude of the velocity aberration in microradians for the Apollo Lunar array with 100 cube corners.

B. Comparison of Apollo with a single cube corner

Comparison with hollow cube,
Dihedral angle offset .5 arcsec
no polarization effects

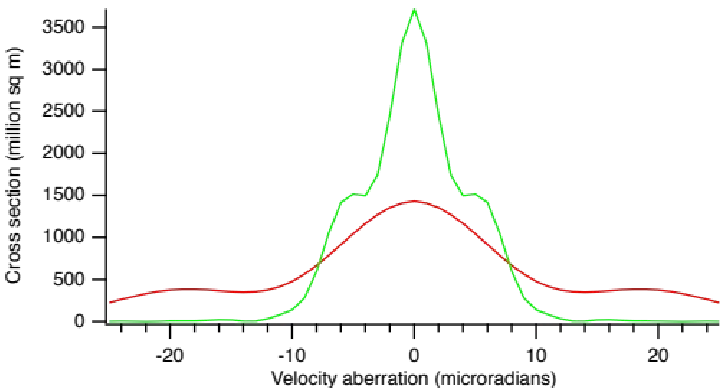

Figure 19. Comparison of Apollo (red)with a hollow cube corner (green) with a .5 arcsec dihedral angle offset (Figure 4.b), wavefront deviation γ = 3.96 microradians.

Comparison with hollow cube,
dihedral angle offset 1.0 arcsec
No polarization effects

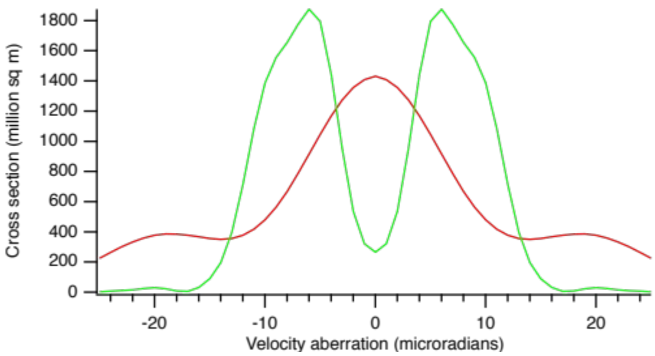

Figure 20. Comparison of Apollo (red) with a hollow cube (green) with a dihedral angle offset of 1.0 arcsec (Fig 8.b), wavefront deviation γ = 7.92 microradians.

Comparison with uncoated 5 inch and 4 inch cubes
Dihedral angle offset .5 arcsec,
circular polarization 1

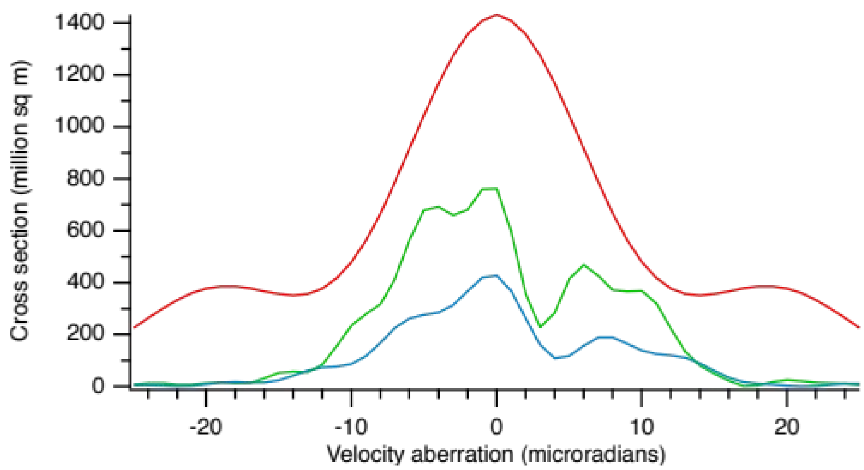

Figure 21. Comparison of Apollo (red) with an uncoated cube (green = 5 inch, Figure 6.b), (blue = 4 inch, Figure 6.f) with a 0.5 arcsec dihedral angle offsets, polarization 1, wavefront deviation γ = 5.78 microradians, and circular polarization 1.

Comparison with uncoated cube,
Dihedral angle offset 1.0 arcsec
circular polarization 1

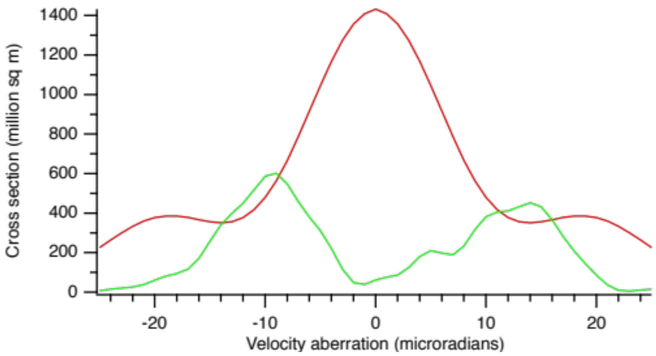

Figure 22. Comparison of Apollo (red) with an uncoated cube (green) with a 1.0 arcsec dihedral angle offset (Fig 10.b), wavefront deviation γ = 11.57 microradians, and circular polarization 1. γ is larger than the velocity aberration for ranging from Earth to the Moon.

Comparison with uncoated cube,
dihedral angle offset 1.0 arcsec
horizontal polarization

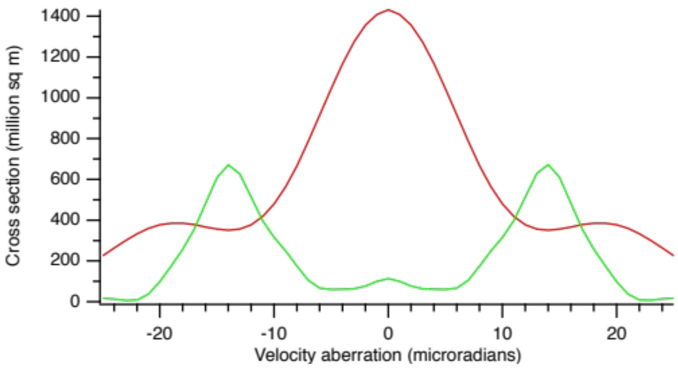

Figure 23. Comparison of Apollo (red) with an uncoated cube (green) with a 1.0 arcsec dihedral angle offset (Figure 14.b), wavefront deviation γ = 11.57 microradians, and linear horizontal polarization. γ is larger than the velocity aberration for ranging from Earth to the Moon.

Comparison with uncoated cube,
dihedral angle offset 1.0 arcsec,
vertical polarization

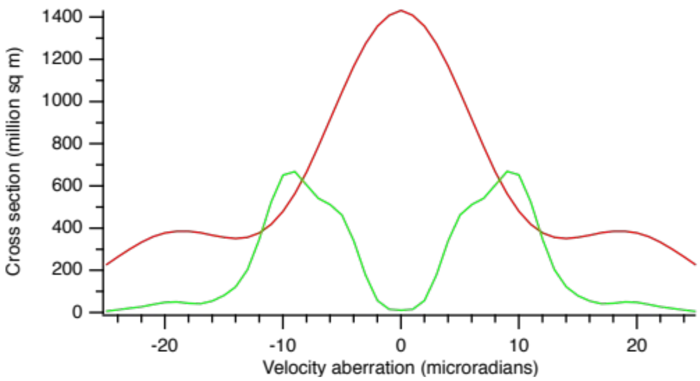

Figure 24. Comparison of Apollo (red) with an uncoated cube (green) with a 1.0 arcsec dihedral angle offset (Fig 15.b), wavefront deviation γ = 11.57 microradians, and linear vertical polarization. γ is larger than the velocity aberration for ranging from Earth to the Moon.

Section 5. GNSS (Global Navigation Satellite Systems) and Geostationary

A large hollow retroreflector could also be used in high earth orbit for GNSS and geostationary satellites,

GNSS Satellites use large planar arrays of small retroreflectors. For off normal incidence angles, GNSS satellites have all of the same problems with pulse spreading as the Apollo Lunar retroreflector arrays. The arrays are very heavy compared to a large single retroreflector.

The paper, “Single Open Reflector for MEO/GNSS type Satellites. A Status Report” (Neubert, 2011) discusses the possibility of using a single large hollow retroreflector for GNSS satellites. The size studied is 196 mm (about 8 inches). The recommended cross section for GNSS satellites is 100 million sq m. Since the satellites rotate to keep the solar panels aligned with the sun, it is not possible to use a single dihedral angle offset with spots aligned with the orbital velocity vector. The paper uses a diffraction pattern in the shape of a ring at the appropriate velocity aberration. The ring shape can be obtained by using a cone shaped phase front.

The proposed design was not successfully developed. At present, no one has been able to build a stable large hollow retroreflector. If a way can be found to do this, the financial and scientific benefits would be substantial.

Section 6. Conclusions

This paper presents theoretical calculations for a perfect cube corner. In practice, a major problem with large cube corners is thermal effects. The theoretical calculations show that a perfect 5 inch cube corner can give a cross section that is comparable to the Apollo arrays with 100 cube corners. The effect of thermal gradients in a solid cube corner increases rapidly with size. The effect is primarily due to the dependence of the index of refraction on temperature rather than distortion of the shape of the glass. A solid coated cube corner can work well in the dark (the Lunokhod 1 retroreflectors are silver coated), but not when sunlit because of heating of the reflective coating. An uncoated solid cube corner loses cross section because of phase changes due to total internal reflection. The diffraction pattern (cross section) is different for every polarization of the incident laser beam. A hollow cube corner gives the largest cross section. It has a weight advantage over a solid cube corner. A hollow cube corner would be easier to deploy on the moon than the multi-cube Apollo arrays. There are no polarization effects.

Advantages and disadvantages of each type of retroreflector

For a solid coated cube corner the advantages are mechanical stability and no polarization effects. The acceptance angle is larger than for a hollow cube because the laser beam is refracted closer to the normal to the front face when entering the cube corner (Arnold, 1972) figure 5, page 7. The disadvantages include non-uniformity of the quartz and phase changes due to thermal gradients in the quartz. The metal coating on the back faces absorbs sunlight that introduces thermal gradients.

For solid uncoated cubes polarization reduces the signal strength and produces complicated diffraction patterns. The advantage is no metal coatings to absorb sunlight. The acceptance angle depends on the azimuth angle of the incident beam (Arnold, 1979), figure 38, page 54. The effect of loss of total internal reflection is shown in more detail for the Lares-1 satellite (Arnold, 2015) figures 6.1 and 6.2. The cutoff angle is between 17 and 57 deg. The cutoff angle for an Apollo cube corner is shown in (Arnold, 2005) figure 4. The Apollo cubes are recessed which limit the acceptance angle to 30 degrees.

The advantage of a hollow cube is that there is no quartz that may be non-uniform and have thermal gradients. A single large hollow cube can be used whenever the incidence angle is within the acceptance angle of the hollow cube and there is adequate signal. For a circular hollow retroreflector the absolute cutoff angle is 35 degrees. Existing designs have not been able to provide a thermally stable large hollow cube corner.

At the present time, there are only a few stations that can do optical laser ranging to the Moon. The NGLR and MoonLIGHT retroreflectors are designed to provide the highest signal that can be obtained from a large uncoated solid retroreflector. If higher signal is needed, the only option would be a large hollow retroreflector.

Unpublished new design

In my opinion, there is a way to build a workable large hollow cube corner using a new, unpublished, proprietary design developed in 2019. No new technology is required. The change is very simple. Building and testing a prototype under thermal vacuum conditions would make it possible to determine the thermal stability of the new design. If the design is thermally stable the size could be increased to provide a larger signal. Eliminating the polarization increases the signal even without increasing the size.

The new developments at Lishan SLR Station of National Time Service Center(NTSC)

Xiao Wang, Shengkai Zhang, Jing Zhang , Jie Liang,
Weichao Li, Xuhai Yang

Email: wangxiao@ntsc.ac.cn

2025.05.22

National Time Service Center, Chinese Academy of Sciences(NTSC,CAS)

CONTENTS

Introduction 01

02 Observation

Summary 03

1.Introduction

➢ Lishan Satellite Laser Ranging Station

Location ： **lintong, Xi'an, Shaanxi (34.5°N 109.2°E)**

SLR station at the top of the Lishan Mountain

1.Introduction

➢ Lishan Satellite Laser Ranging Station

Equipment	Parameters
Telescope	receive aperture: 1.05m
	Azimuth tracking speed: 3"/s~4°/s Elevation tracking speed: 3"/s~2°/s
	Pointing Accuracy: ≤ 3"(after pointing model)
	Tracking Accuracy: ≤ 1"
Laser	Wavelength:532nm
	Repeat Frequency: 0.1kHz~1kHz
	Pulse Width: ≤ 25ps
Detector	APD
Timer and Frequency	Time Stability: 3.5ns@10000s Frequency stability: 2×10^{-12}@1000s
Calibration	In the telescope Accuracy: ≤7mm

2.Observation

Observed Satellite

until now , it has observed about 100 satellites.

Orbit Altitude	Satellites Name	Precise
LEO	Gracefo-1 、 Gracefo-2 、 Stella 、 Ajisai 、 Lares 、 Jason-3 、 Beacon-C 、 Cryosat-2 、 Sentinel-6A 、 Hy-2B 、 Hy-2C 、 Hy-2D 、 Larets 、 Saral 、 Starlette 、 CSS(468km) 、 Westpac 、 Paz 、 Swarmc	0.5~1cm AJ: 1.5~2cm
MEO	Lageos-1 、 Lageos-2 、 Etalon-1 、 Etalon-2 、	L1/L2 ： ~1cm E1/E2 ： 3~5cm
	BDS ： M1 、 M2 、 M3 、 M4 、 M5 、 M6 、 M9 、 M10 、 M11 、 M12 、 M13 、 M14 、 M15 、 M16 、 M18 、 M19 、 M20 、 M21 、 M22 、 M23 、 M24 、 Compass-M3 、 GLONASS: 105 、 106 、 116 、 127 、 128 、 129 、 131 、 132 、 133 、 134 、 137 、 138 、 139 、 140 、 141 、 142 、 143 、 144 、 146 、 GALILEO ： 101 、 102 、 103 、 104 、 201 、 203 、 204 、 205 、 206 、 207 、 208 、 209 、 210 、 211 、 212 、 214 、 215 、 216 、 217 、 218 、 219 、 220 、 221 、 222 、 223 、 224 、 225 、 227	2~3cm
GEO	COMPASS:I3 、 I5 、 I6B 、 G8; QZSS ： QZS2 、 QZS3 、 QZS4 、	2~3cm

2.Observation

Observed Satellite

Lageos1/2 and Lares from March to April

Month	Name	Passes	NP Total	Minutes of data	RMS（average,mm）
March	Lageos1	6	26	42.8	11.8
	Lageos2	3	18	31.1	8.7
	Lares	6	55	27.1	7.2
April	Lageos1	8	47	87.1	9.9
	Lageos2	10	46	81.5	9.98
	Lares	1	12	7.0	6.1

2.Observation

Observed Satellite

Lageos1

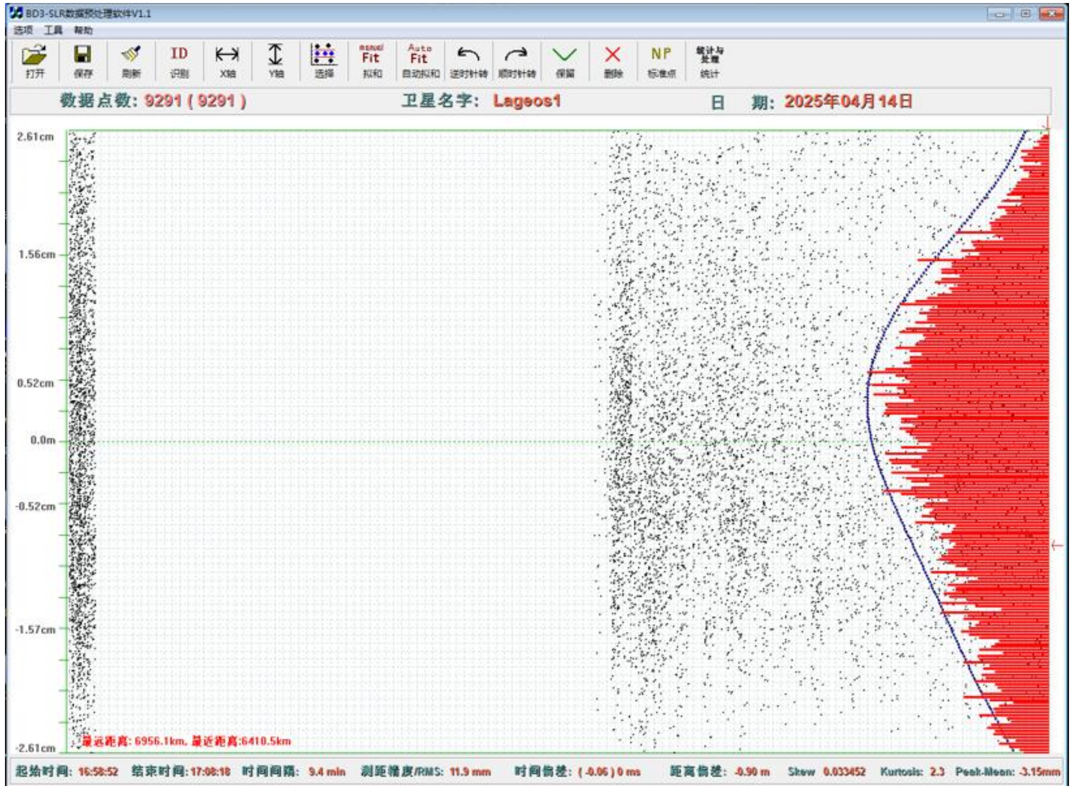

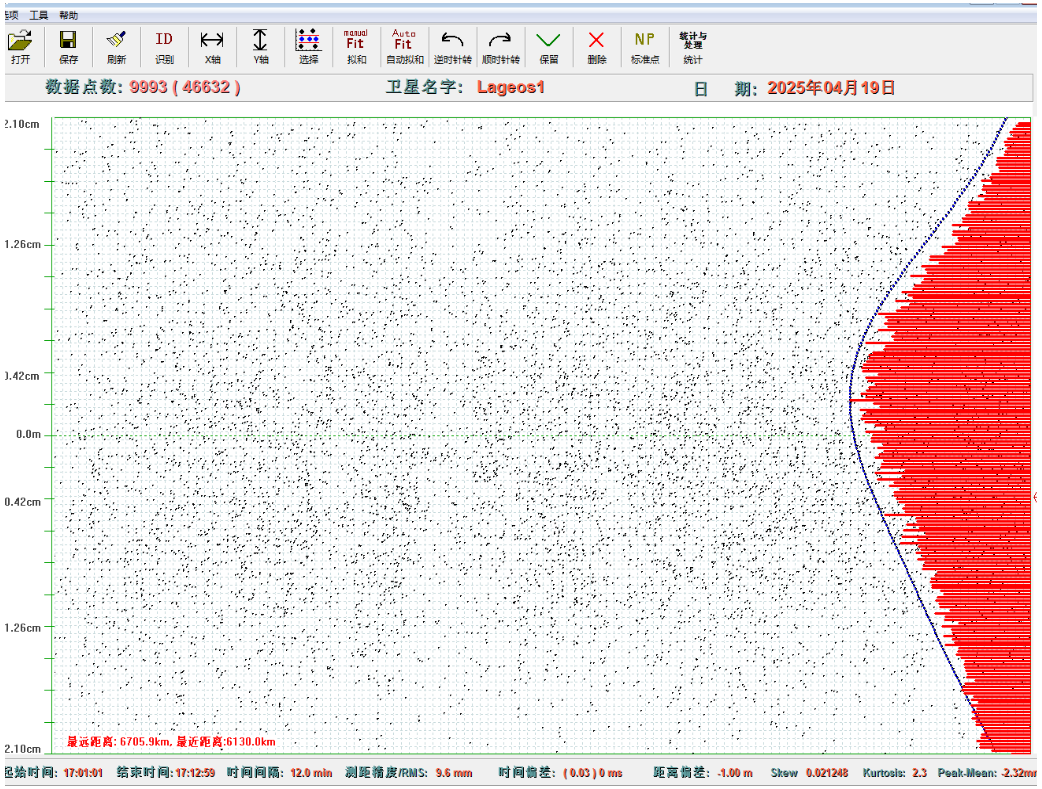

2.Observation

Observed Satellite

Lageos2

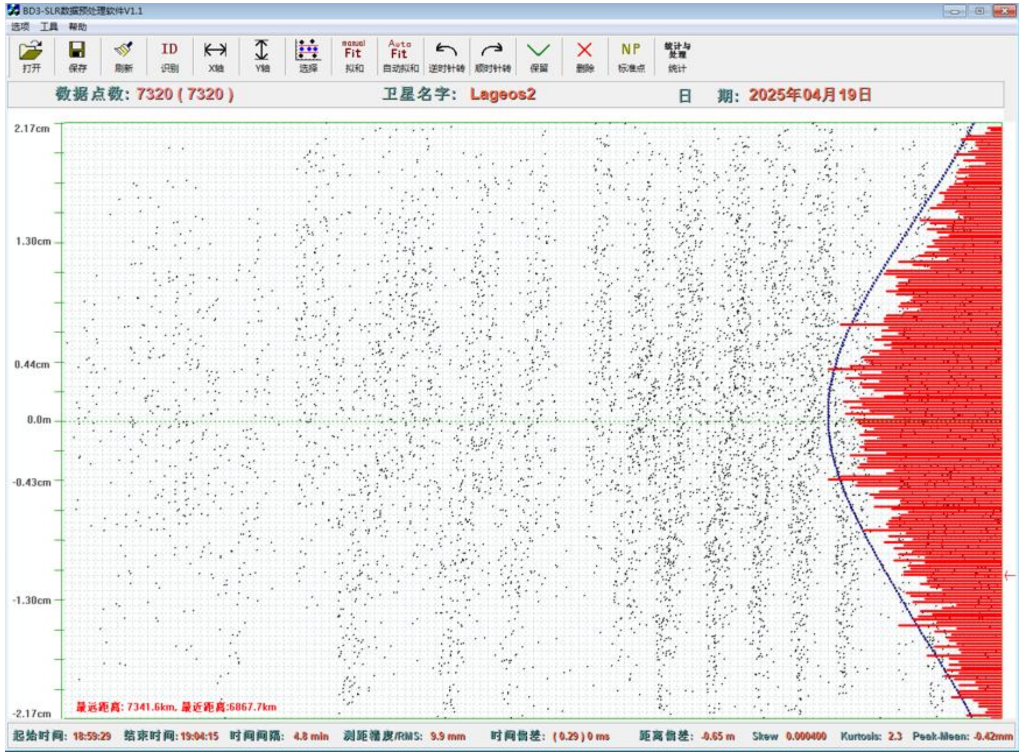

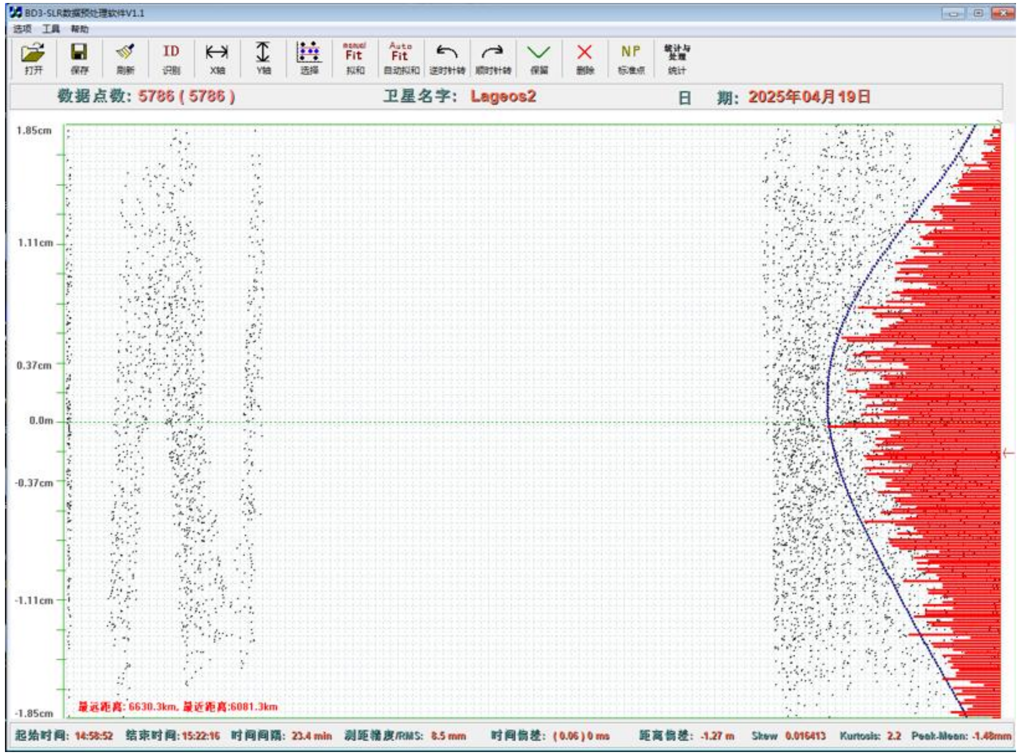

2.Observation

Observed Satellite

Lares

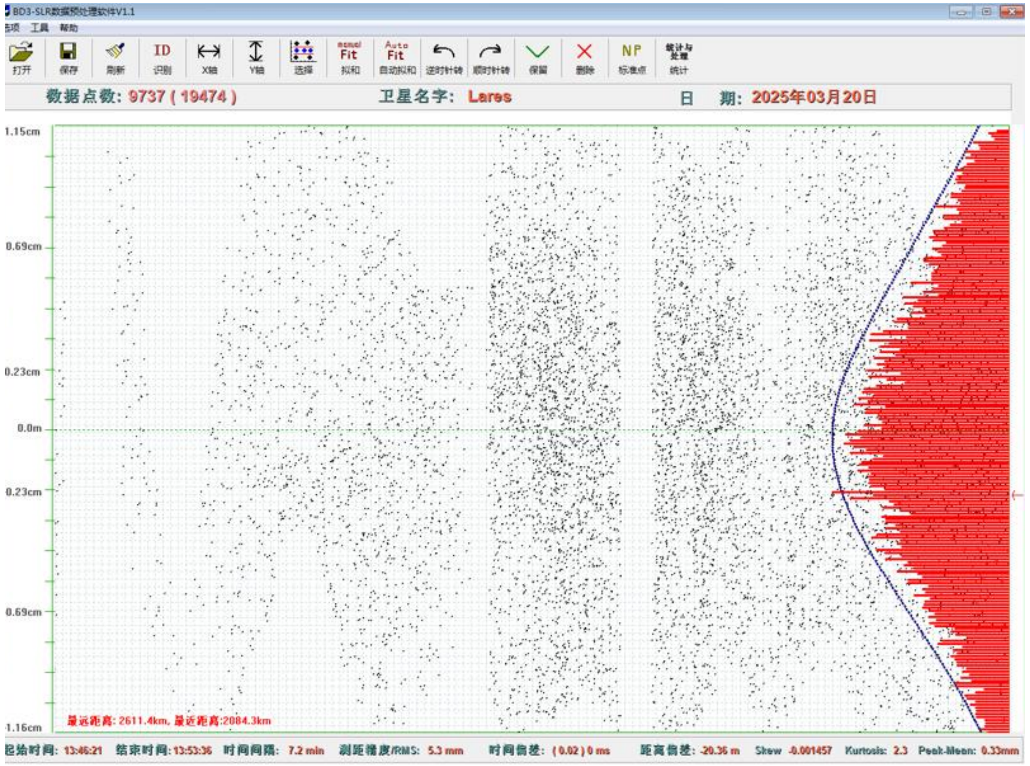

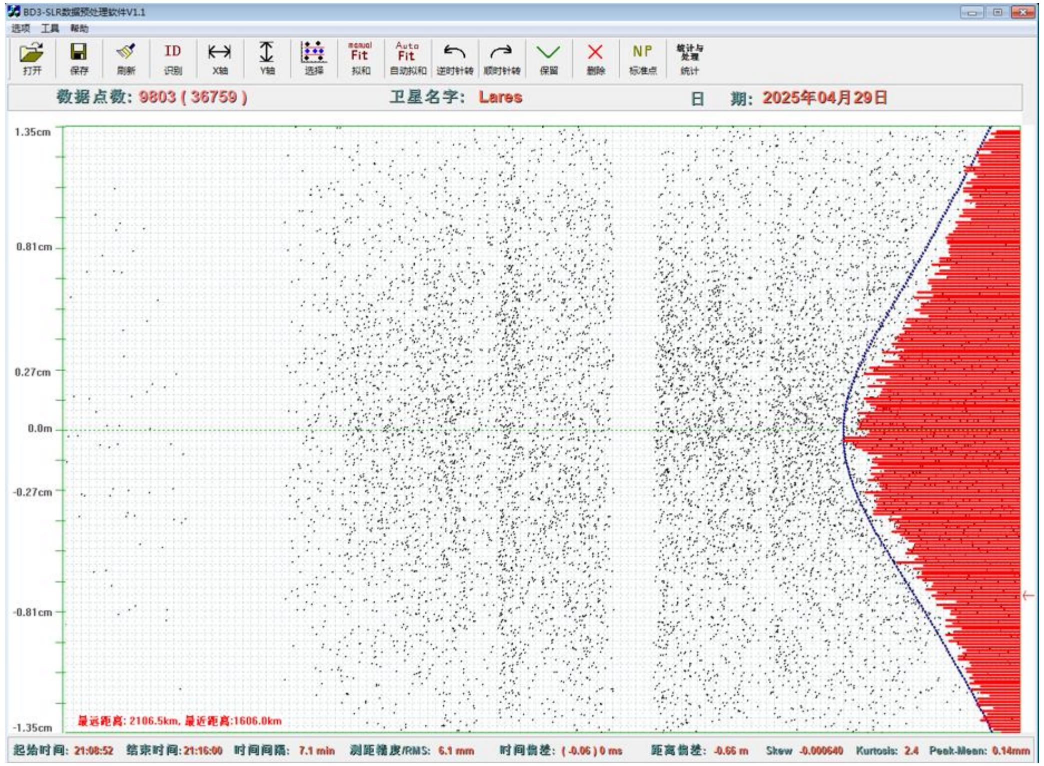

2.Observation

Coordinate Estimate

Geometric Methods （ Multiple epochs and Multiple satellites ）

$$\rho_{SLR,i} = \sqrt{[X_i - x]^2 + [Y_i - y]^2 + [Z_i - z]^2} + \Delta\rho_{sys} + \Delta\rho_{trop} + \Delta\rho_{rel} + \Delta\rho_{LRA} + \varepsilon$$

(x, y, z)—**station coordinate**

(X, Y, Z)—**satellite orbit**

After errors correction, like system delay, Tropospheric delay, COM， and others

2.Observation

Coordinate Estimate

Measurement Model:

Center of Mass(m)	0.251
System Delay	Target Calibration
Model for Tropospheric	IERS2010
Relativistic Effects	
Station deformation(Tide)	
Minimum Elevation(deg)	10

2.Observation

Coordinate Estimate

Satellites Used (last year data)

Satellite	Observed Date	Observed Time(UTC)	Elevation	NP
Lageos1	2024.09.23	13:13—13:22	54°—81°	6
	2024.09.24	12:18—12:27	13°—33°	5
	2024.09.24	15:20—15:31	22°—32°	6
	2024.10.10	14:41—14:56	23°—33°	7
	2024.10.13	10:53—11:01	39°—54°	5
	2024.10.13	14:21—14:32	33°—42°	7
	2024.11.05	11:25—11:35	15°—40°	6
	2024.11.06	13:01—13:10	19°—34°	6

Satellite	Observed Date	Observed Time(UTC)	Elevation	NP
Lageos2	2024.09.22	11:46—11:55	23°—28°	5
	2024.09.22	15:52—16:03	36°—59°	6
	2024.09.24	12:10—12:17	18°—26°	2
	2024.10.10	13:54—14:02	38°—56°	5
	2024.10.10	17:44—17:57	40°—55°	7
	2024.10.13	15:41—15:52	13°—30°	6
	2024.11.04	14:21—14:31	26°—42°	6
	2024.11.05	20:56—21:04	36°—37°	5
	2024.11.06	11:01—11:10	25°—44°	6
	2024.11.06	14:32—14:40	19°—34°	5
	2024.11.06	19:14—19:25	39°—64°	6
	2024.11.08	11:16—11:25	22°—41°	5

20 passes, 112 NP

2.Observation

Coordinate Estimate

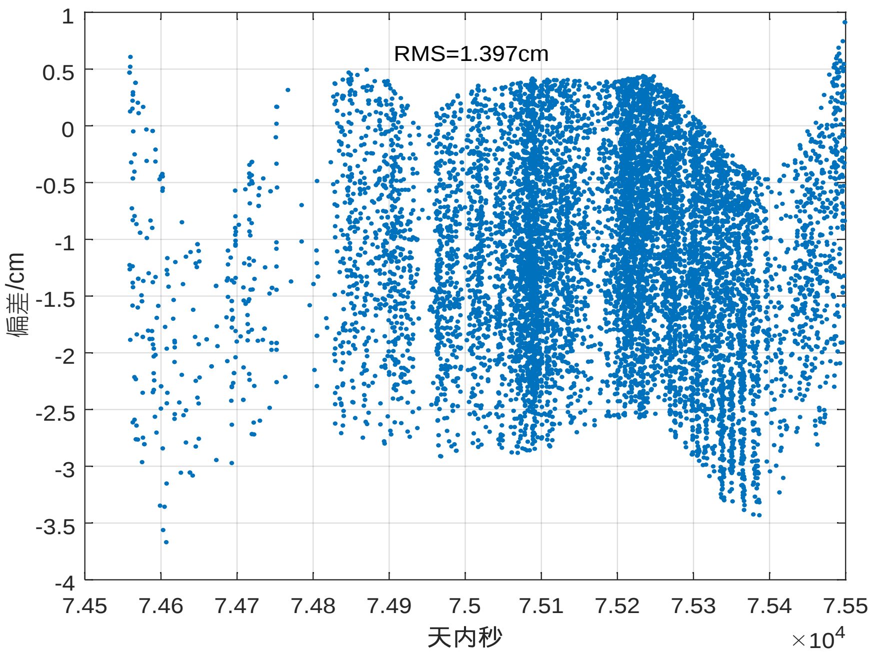

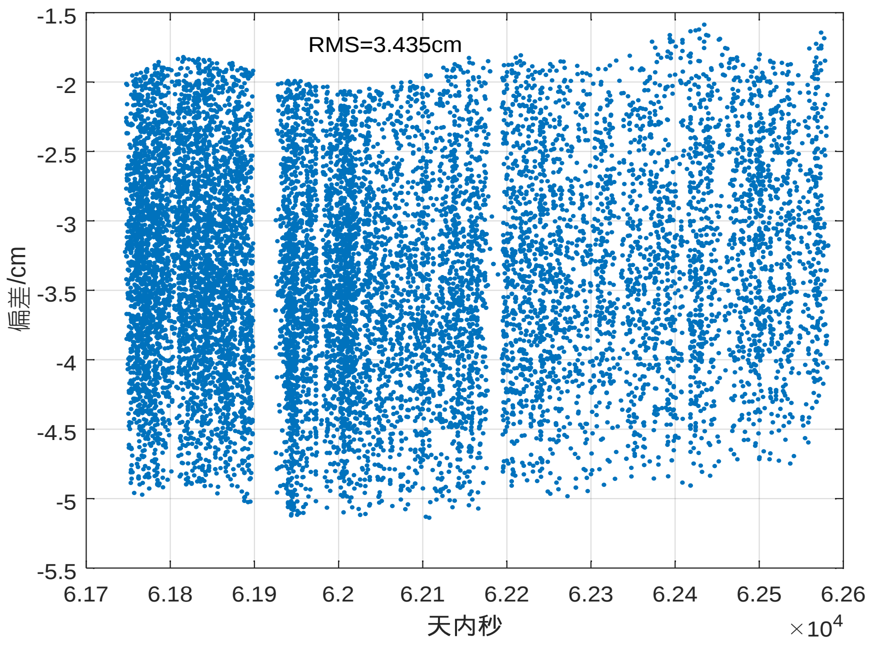

Will observe more data to coordinate estimate.

3.Summary

Lishan SLR Station in Observation

- More than 90% satellites in Current Mission have been observed
- Measurable Range: 500km~38000km
- Lageos1/Lageos2/Lares Precision: ~1cm
- other satellites precision: 1~3cm
- coordinate precision: 1~3cm

3.Summary

Next Step

- Conducting routine daytime and night observations, there is only a little daytime observation data;
- observe more data to monitor the station's position changes
- EOP Determination;
- …

Welcome to visit and guide to Lishan SLR station ！

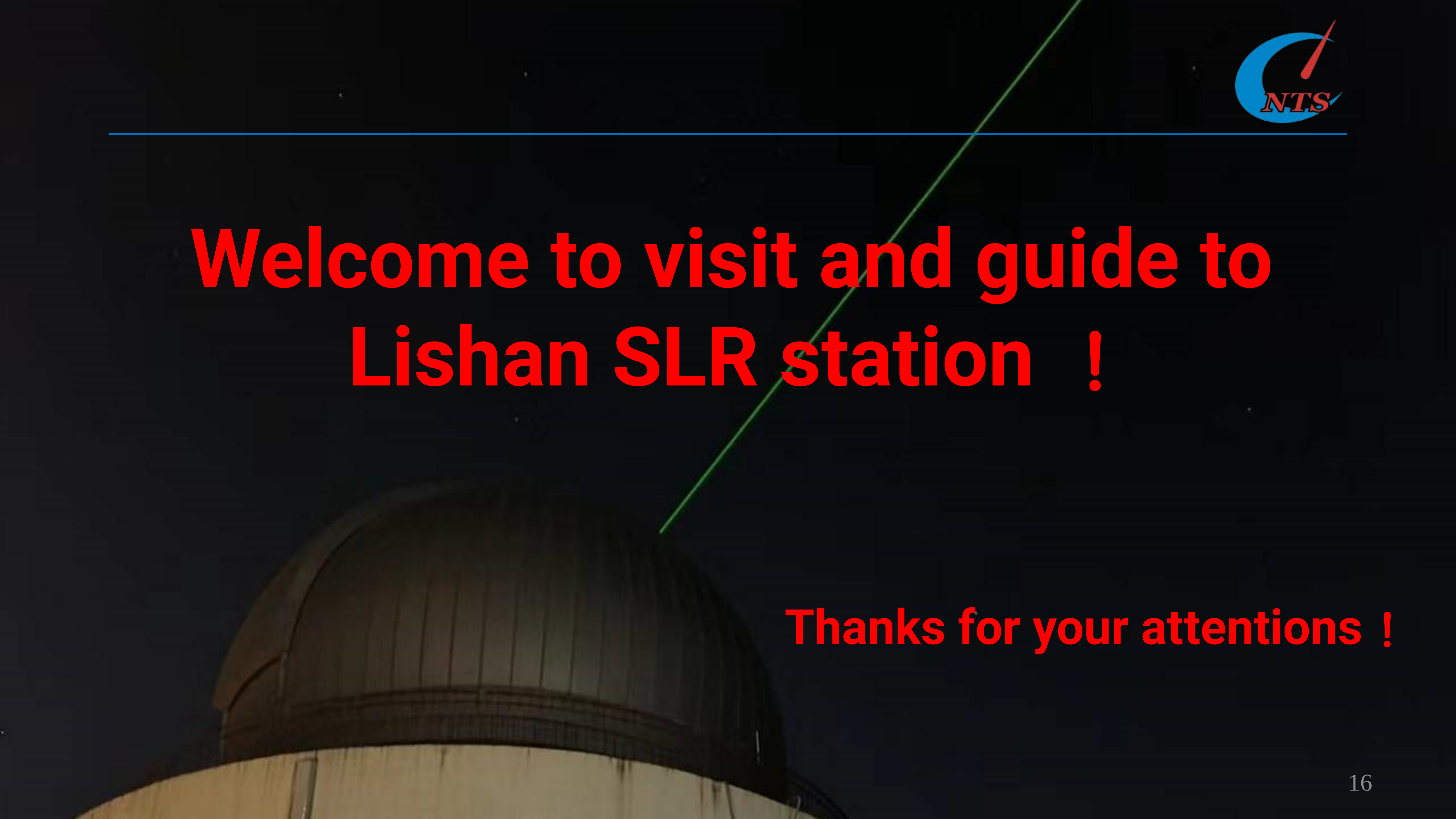

Thanks for your attentions！

Matthew Wilkinson, Robert Sherwood, Toby Shoobridge

Installing a New PI Laser at SGF, Herstmonceux

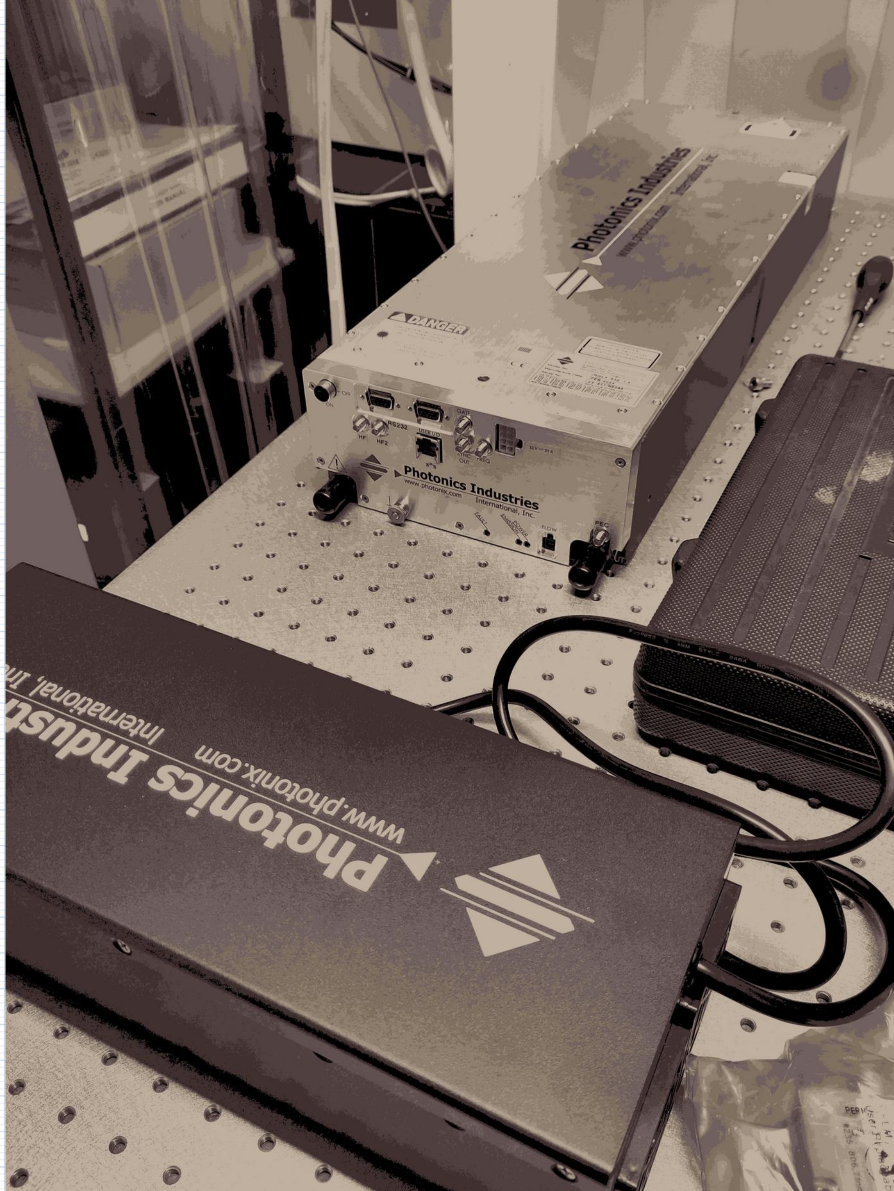

British
Geological
Survey

High-Q kHz SLR

The Space Geodesy Facility, Herstmonceux, UK began kHz SLR in **2008** using a High-Q 2kHz, 10ps, 0.4mJ laser.

The laser was later redesigned and it became much more reliable, firing at 1kHz, with 1mJ pulses. It enabled SLR observations on all ILRS targets.

In recent years, service maintenance has become less available and replacement components are now scarce.

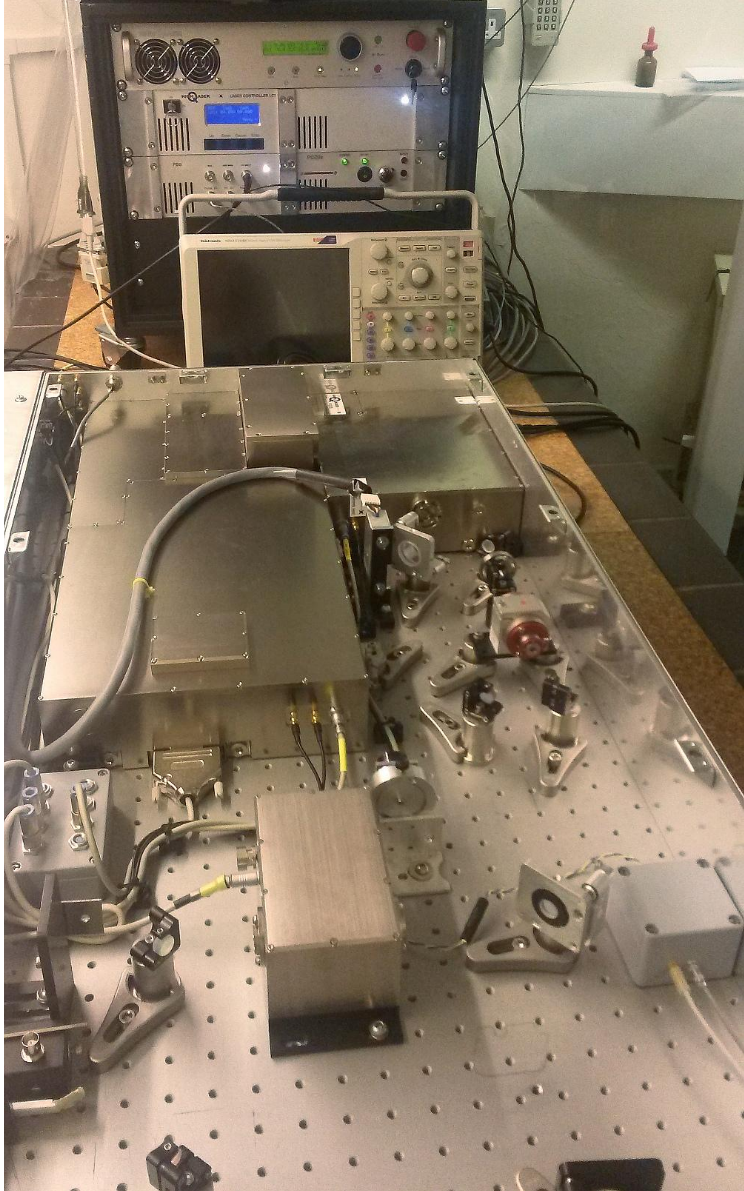

High-Q kHz SLR

In early 2023, we discovered a coolant/water breach in the laser amplification diode unit.

Fortunately, the diode had exceeded it's life expectancy and we already had a spare. However, another replacement diode was not available to purchase.

So we began to look for a new laser to take over daily operational SLR observations.

Replacement kHz SLR

A tendering call in early 2023 had our required specifications, which included:

- Wavelength @ exit 532 ± 1 nm
- Pulse length 8–25 ps FWHM @ 532 nm
- Repetition rate 1 kHz
- Pulse energy > 1 mJ @ 1 kHz
- Timing jitter < 6 ns
- Beam quality $M^2 < 1.5$ diffraction limit
- Output stability < 2% RMS
- Warm up time < 20 minutes
- Line width must be specified

Additional credits:

- Ability to transmit either 1064 or 532 nm wavelength
- Ability to fire at higher rates up to 10kHz
- Ability to fire at different repetition rates without optical realignment

Photonics Industries kHz SLR

It was decided that we buy a **Photonics Industries (PI) RGLX-532-1.5** laser, with the following spec:

- 1.5 W at 1 kHz 532nm
- Pulse width < 25ps
- Pulse stability < 2% RMS
- Typical $M^2 < 1.3$
- Single shot to 5kHz
- Line width < 75 pm
- 20 minute warm up

Price > £200k

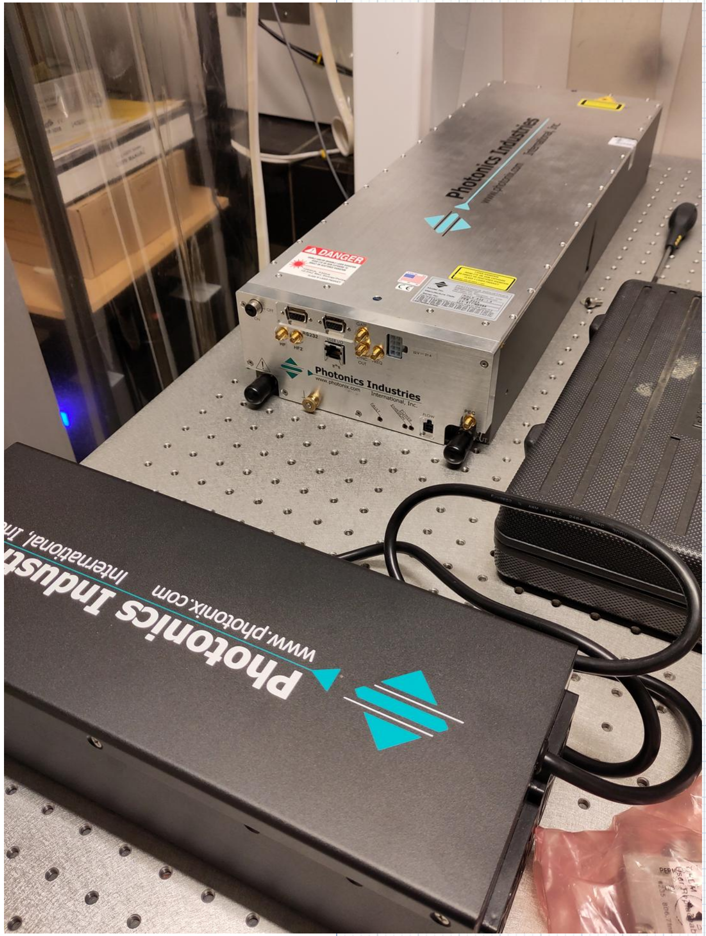

Photonics Industries kHz SLR

The laser is comprised of

- Optical laser unit
- Power Supply
- Laptop running control software
- Large Chiller

No additional Electronic Control Rack

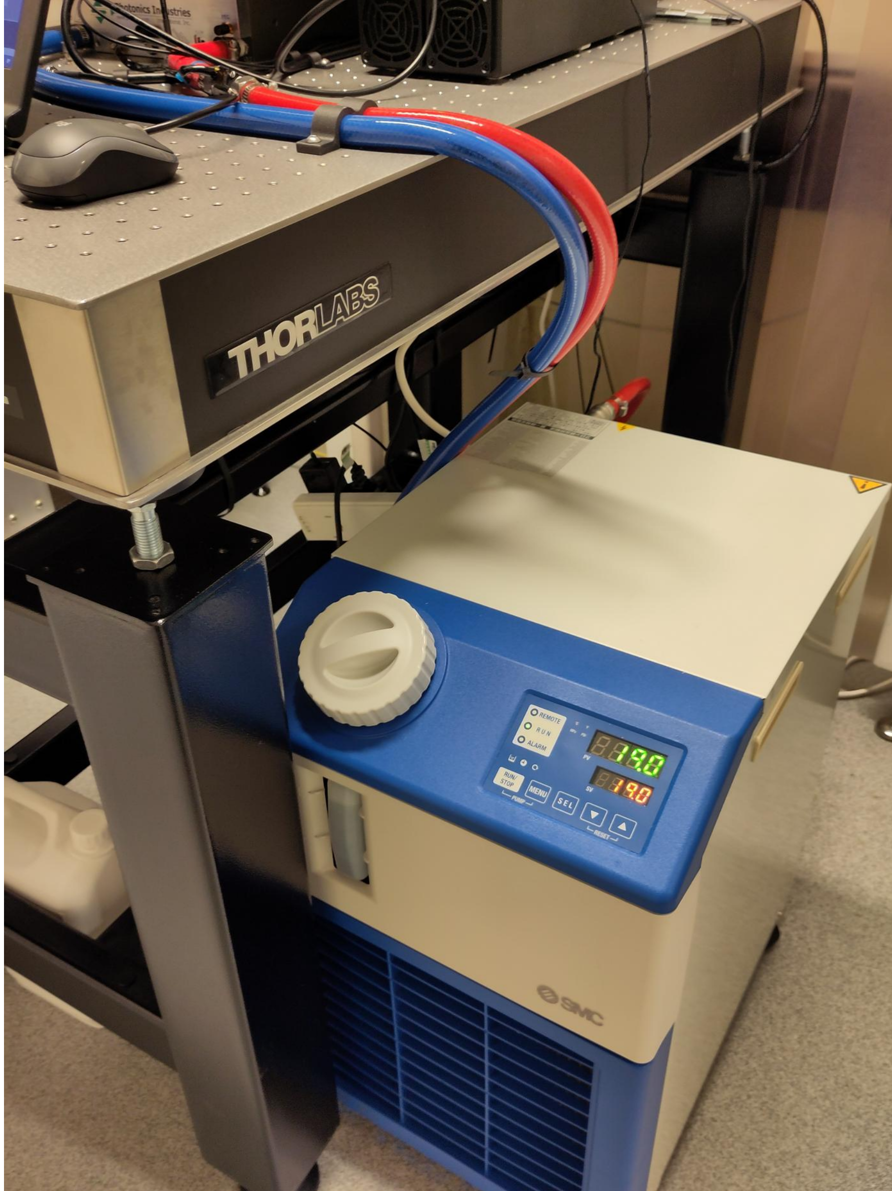

Photonics Industries kHz SLR

It is very compact

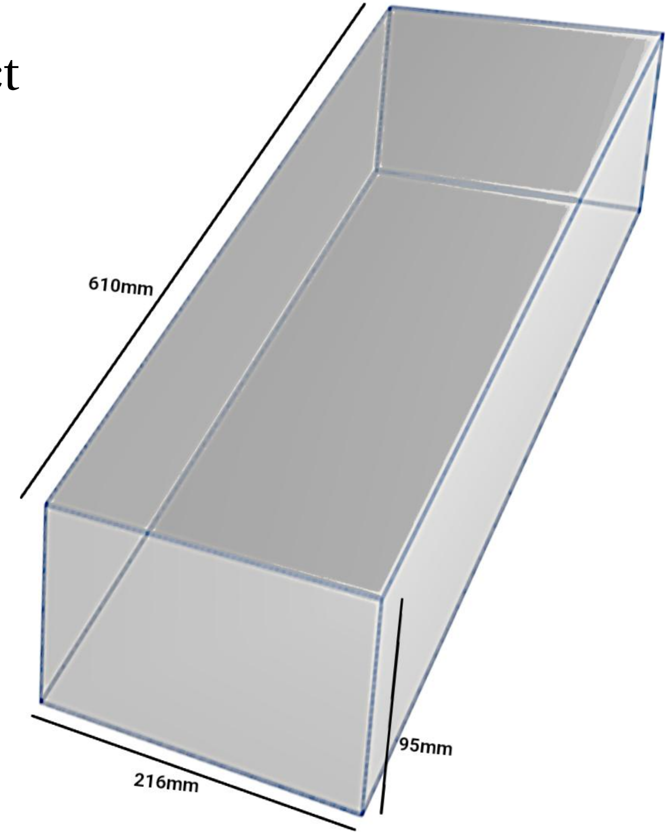

Other Advantages

The PI laser can be operated at higher rates with increasing power up to 5kHz.

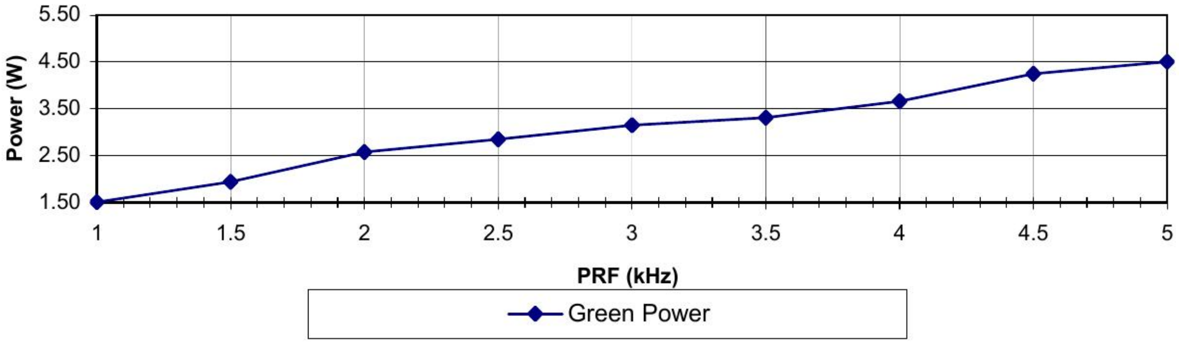

In theory no internal alignment would be needed, but this is currently untested. Instructions are provided to do this through the UI and using different settings files.

For minor issues, remote servicing is available by engineers. This involves remotely connecting to the laser unit and adjusting lenses with motors.

Photonics Industries kHz SLR

The laser was delivered in January 2024 and installed on an empty third laser table for testing.

This location allows for a mirror to direct the outgoing beam in to the coude for alignment.

A start diode is installed outside of the laser unit, instead of using the integrated signal.

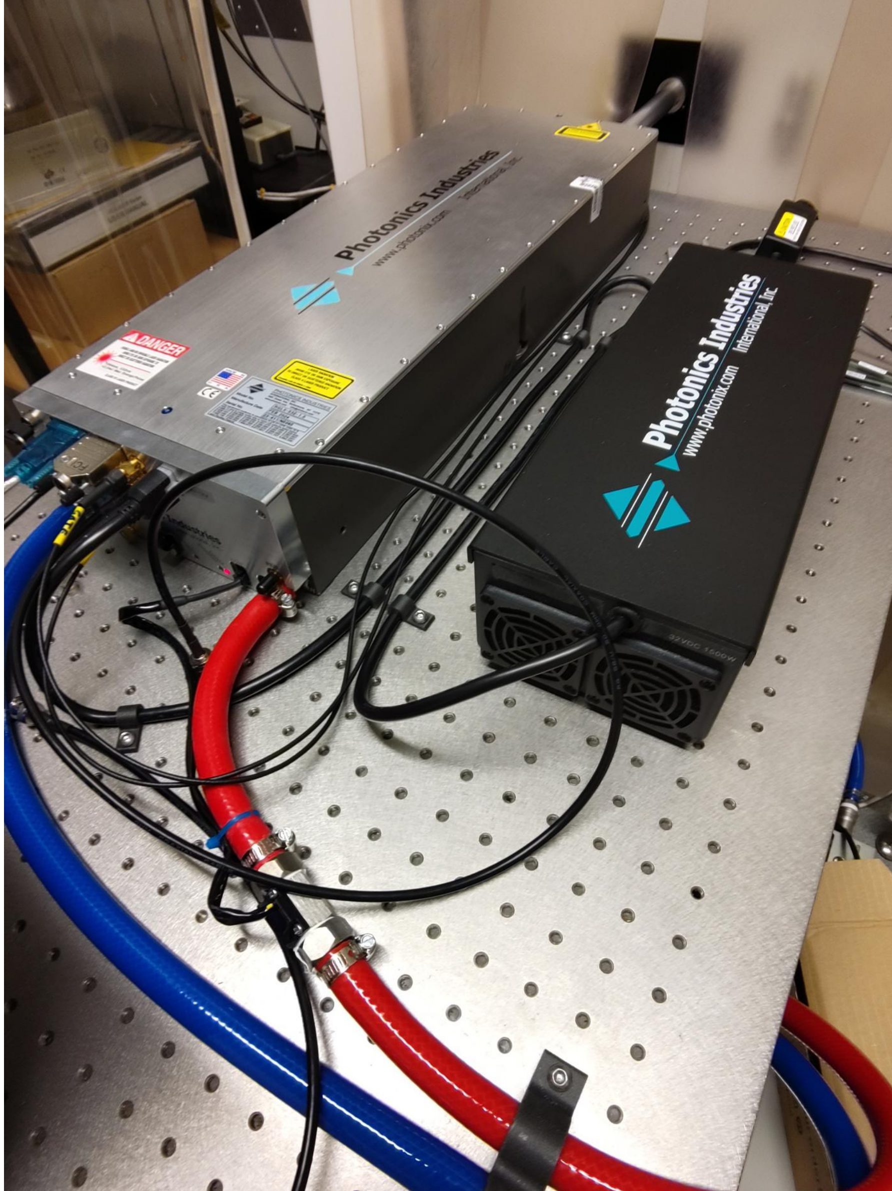

Photonics Industries kHz SLR

Calibrations showed multiple pulses.

These could also be seen using a fast diode coming out of the laser, which confirmed the source.

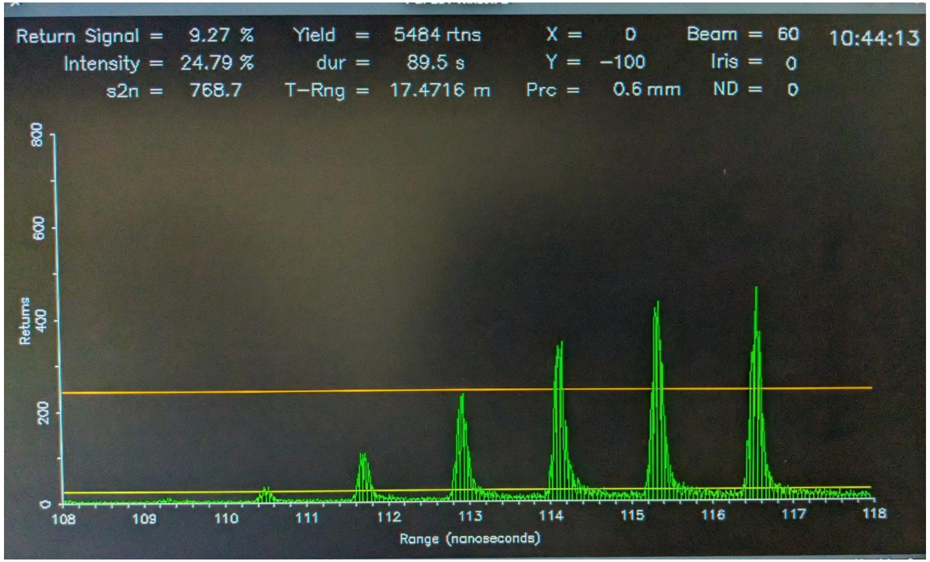

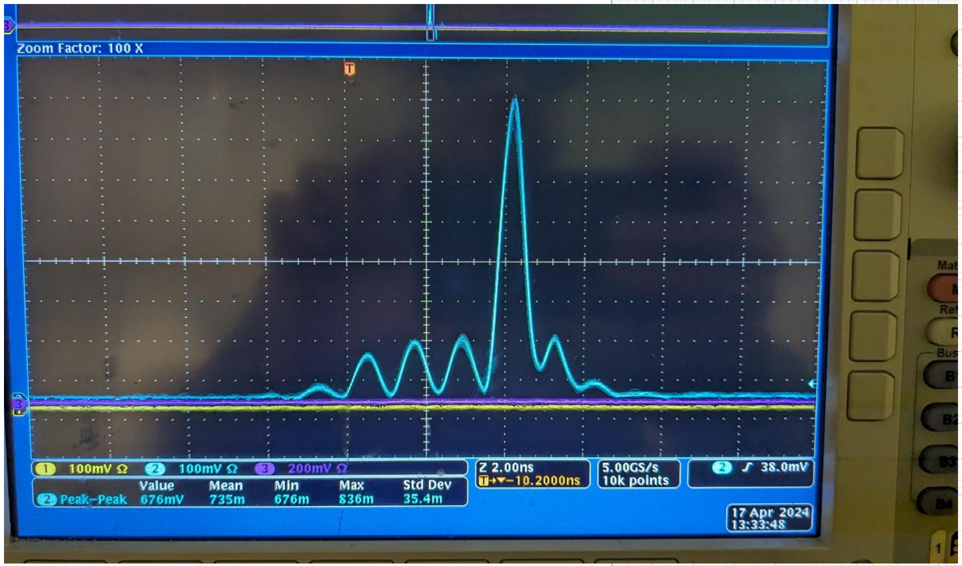

Photonics Industries kHz SLR

After attempting to fix these remotely, the laser was returned to the manufacturer.

Laser damage was discovered, which must have been present when it left the factory. The factory test did not used a fast enough diode.

The laser returned in **September 2024** and the pulses were no longer present.

Photonics Industries kHz SLR

Pulse width spec < 25ps

Photonics Industries laser has a larger calibration RMS.

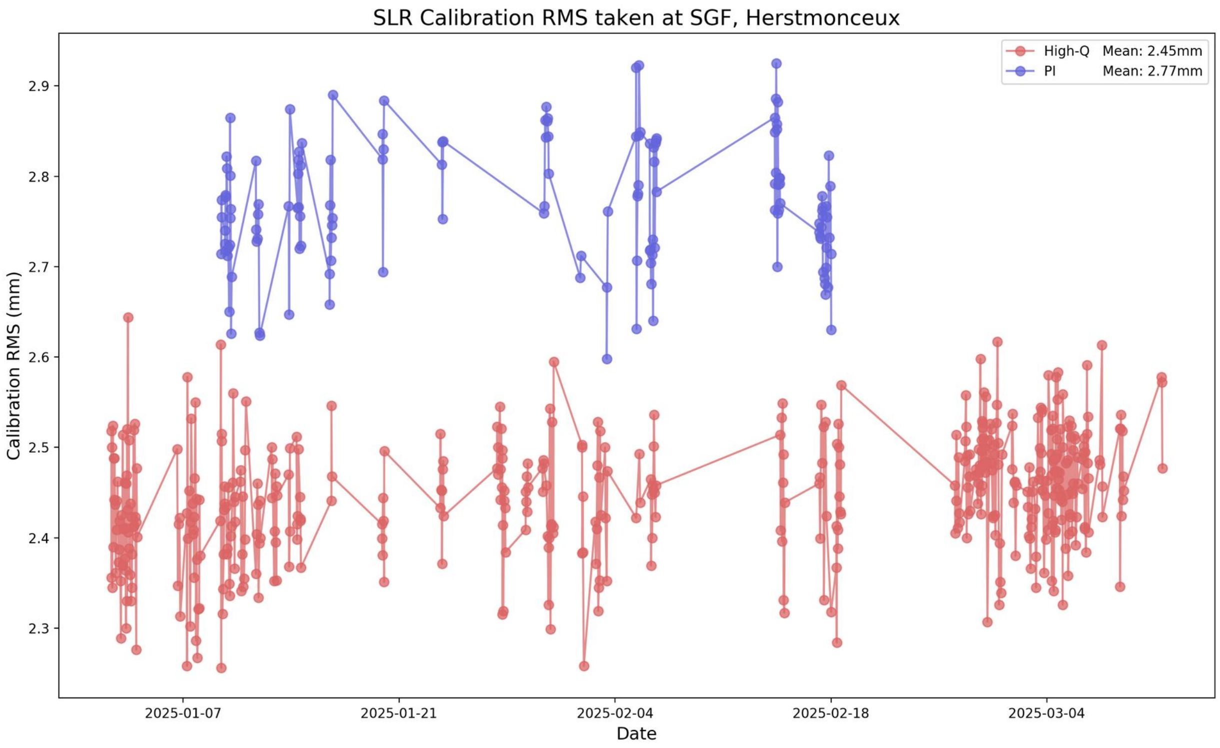

Photonics Industries kHz SLR

Calibration stability is related to temperature.

We are aware of greater variation between calibration values for the PI laser.

This is improved with the laser under a blanket.

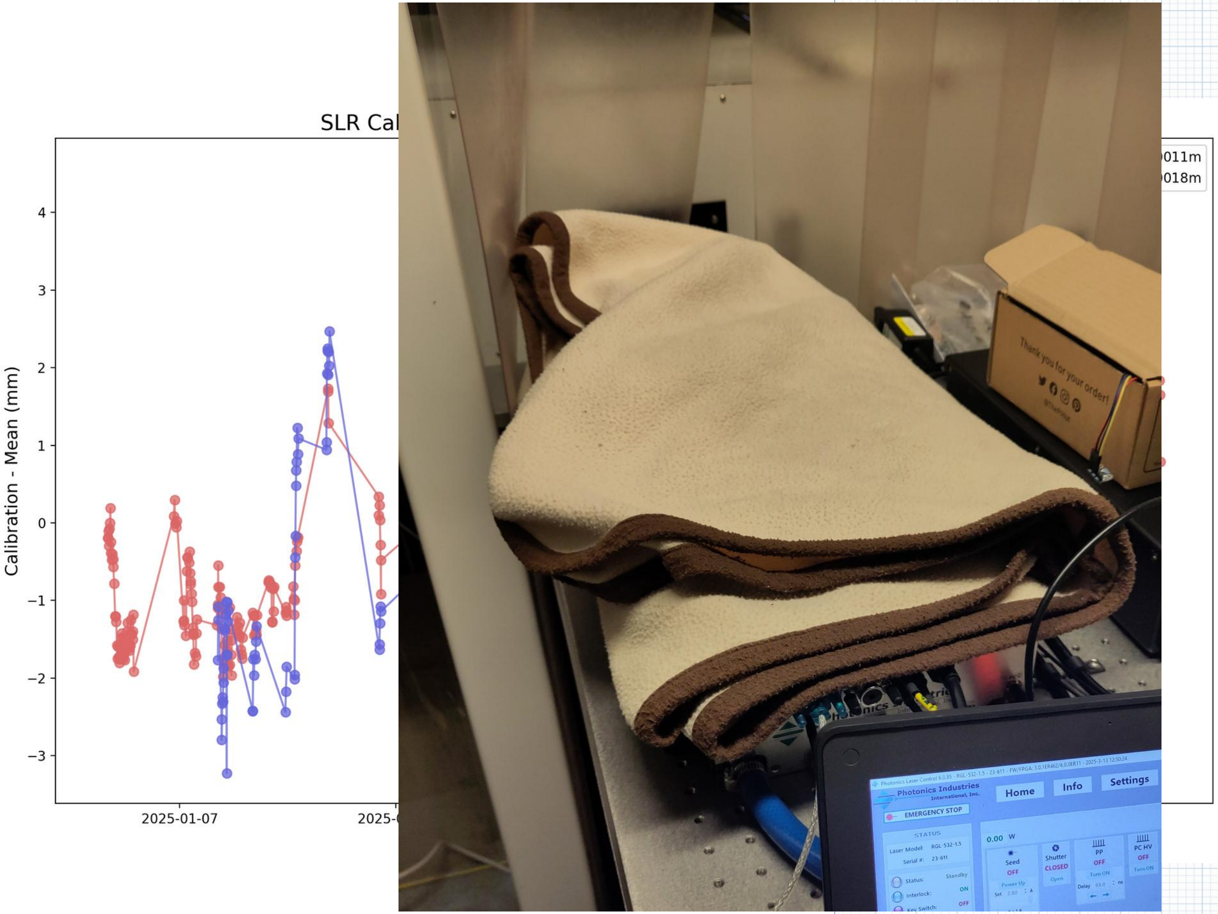

Photonics Industries kHz SLR

The PI laser has been fully integrated in to the SLR system and has been used successfully to track all targets.

The SLR data collected with the new system has been put in to **quarantine** by the ILRS Data Centers and will be analysed for potential biases once sufficient LAGEOS and LARES-2 data has been acquired.

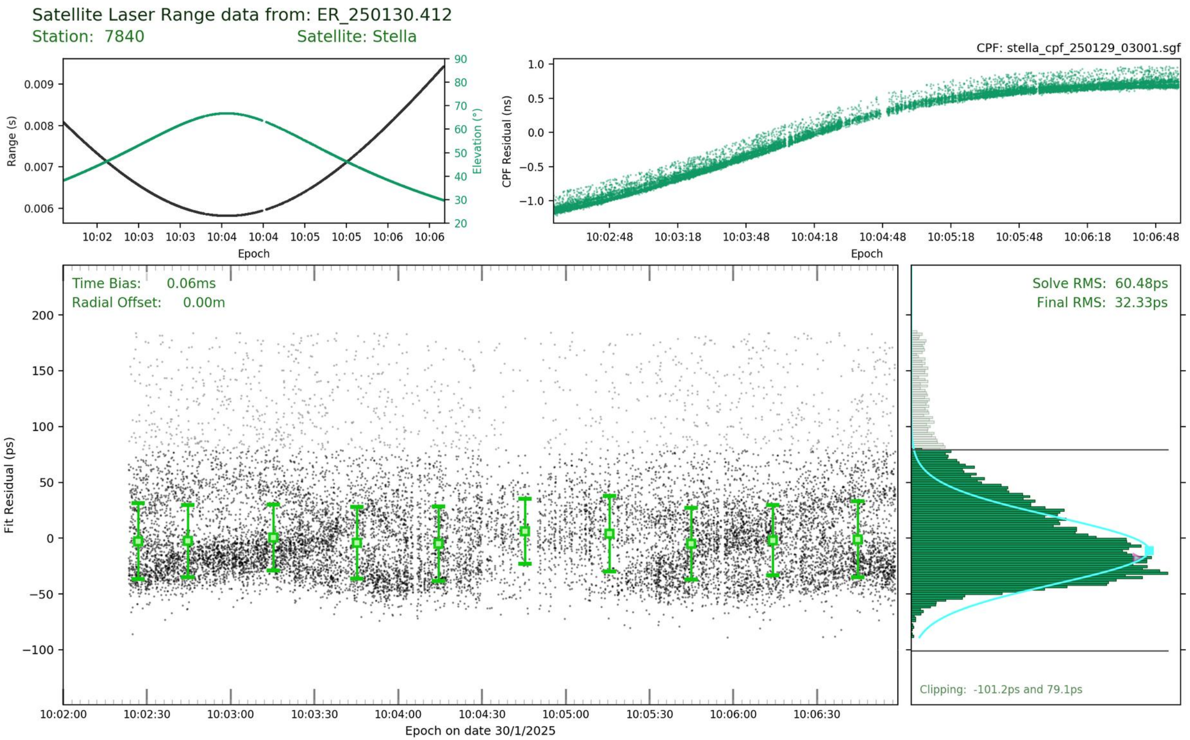

Photonics Industries kHz SLR

The new configuration passed quarantine on 31st March.

A day or so before, the High-Q laser failed and we have yet to get it to come back.

The PI laser has been performing very well during a long period of clear skies for almost 2 months.

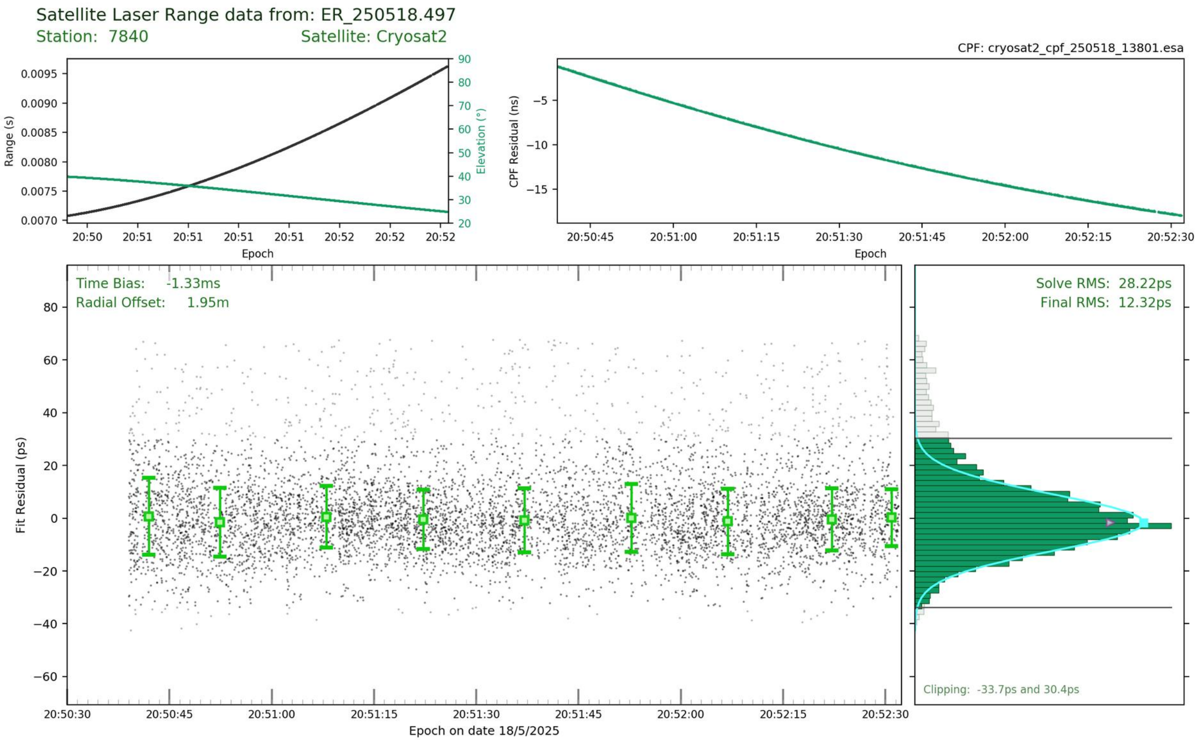

Conclusions

- The **Photonics Industries (PI) RGLX-532-1.5** laser is a good replacement for the long serving High-Q kHz laser.
- Herstmonceux delivered a sample of LAGEOS and LARES-2 passes for quarantine assessment.
- Laser energy is sensitive to ambient temperature and this can result in a range bias. The laser must therefore be kept in a stable environment.

The PI laser will be relocated to the table currently holding the legacy 12Hz laser and it will be inside a temperature stable tent.

END

WESTPAC

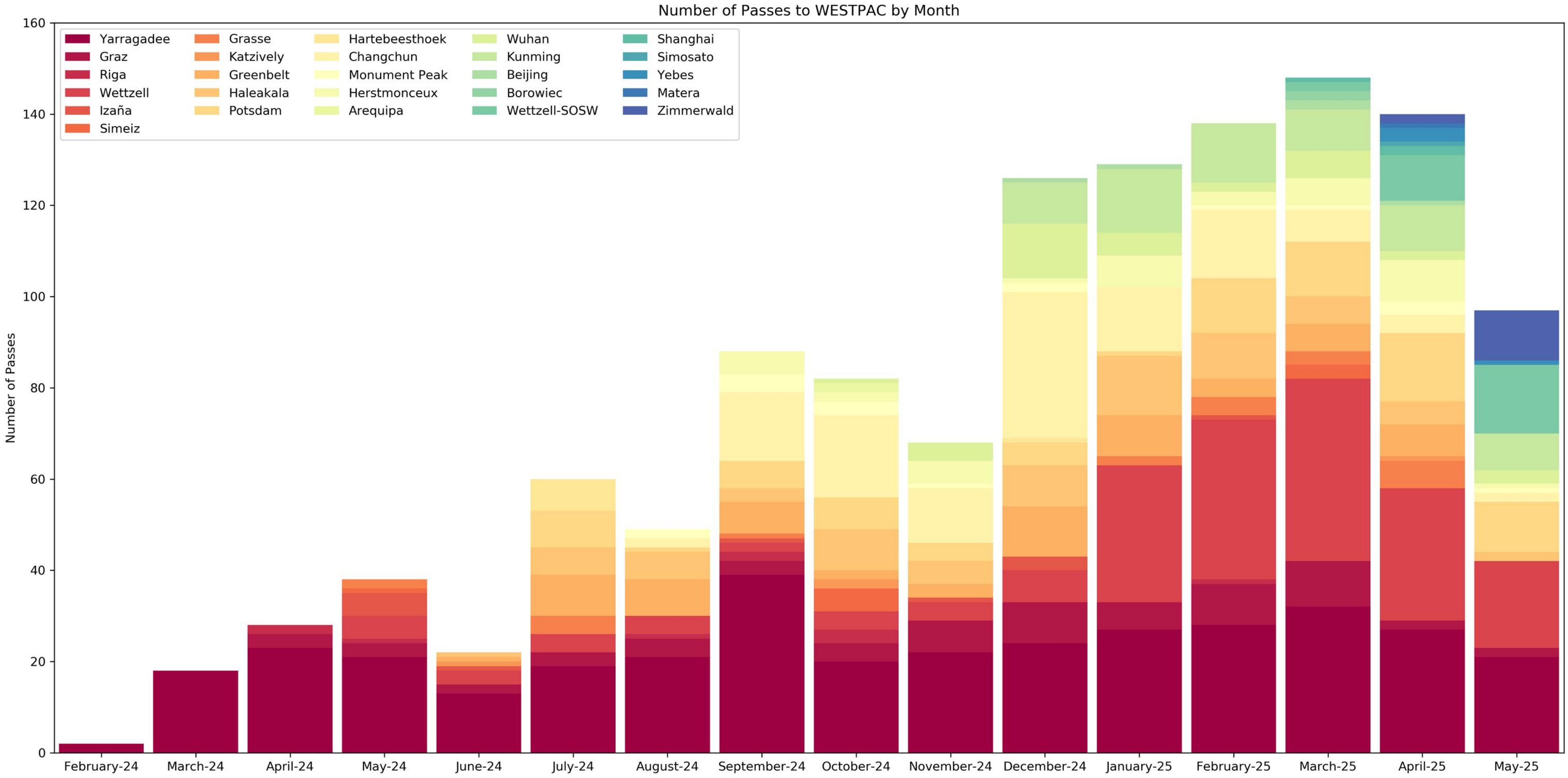

Number of Passes to WESTPAC by Month
Number of Passes
0
20
40
60
80
100
120
140
160
Yarragadee
Graz
Riga
Wettzell
Izaña
Simeiz
Grasse
Katzively
Greenbelt
Haleakala
Potsdam
Hartebeesthoek
Changchun
Monument Peak
Herstmonceux
Arequipa
Wuhan
Kunming
Beijing
Borowiec
Wettzell-SOSW
Shanghai
Simosato
Yebes
Matera
Zimmerwald
February-24
March-24
April-24
May-24
June-24
July-24
August-24
September-24
October-24
November-24
December-24
January-25
February-25
March-25
April-25
May-25

Stella

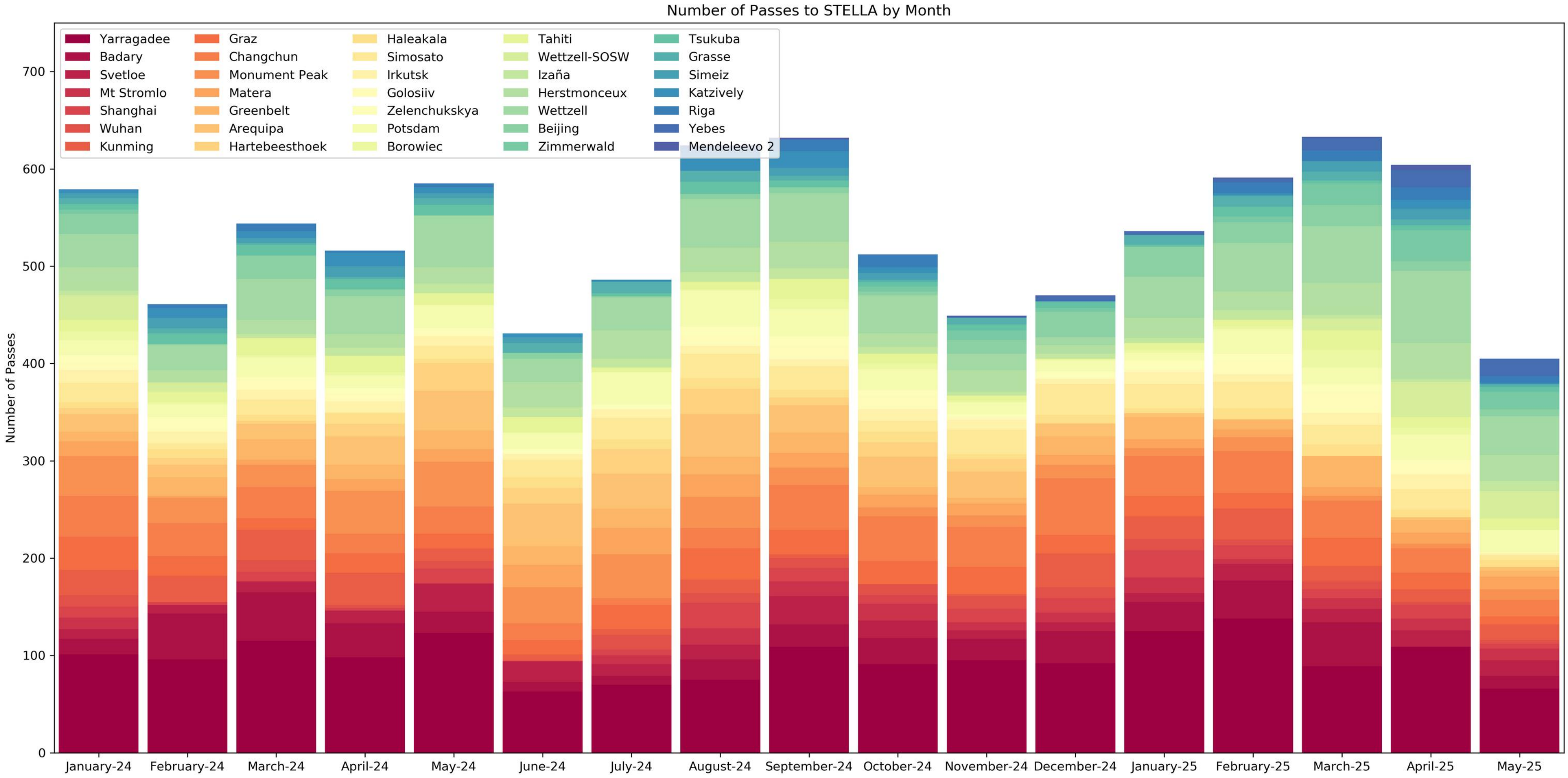

Number of Passes to STELLA by Month
Number of Passes
0
100
200
300
400
500
600
700
Yarragadee
Badary
Svetloe
Mt Stromlo
Shanghai
Wuhan
Kunming
Graz
Changchun
Monument Peak
Matera
Greenbelt
Arequipa
Hartebeesthoek
Haleakala
Simosato
Irkutsk
Golosiiv
Zelenchukskya
Potsdam
Borowiec
Tahiti
Wettzell-SOSW
Izaña
Herstmonceux
Wettzell
Beijing
Zimmerwald
Tsukuba
Grasse
Simeiz
Katzively
Riga
Yebes
Mendeleevo 2
January-24
February-24
March-24
April-24
May-24
June-24
July-24
August-24
September-24
October-24
November-24
December-24
January-25
February-25
March-25
April-25
May-25

Sentinel Report 2024

- GMV published the 2024 Sentinel report here:

https://gmvdrive.gmv.com/index.php/s/dW3kGxJcBNBQ2dF

ACES on the ISS

https://www.esa.int/Science_Exploration/Human_and_Robotic_Exploration/ACES_finds_its_home_in_orbit

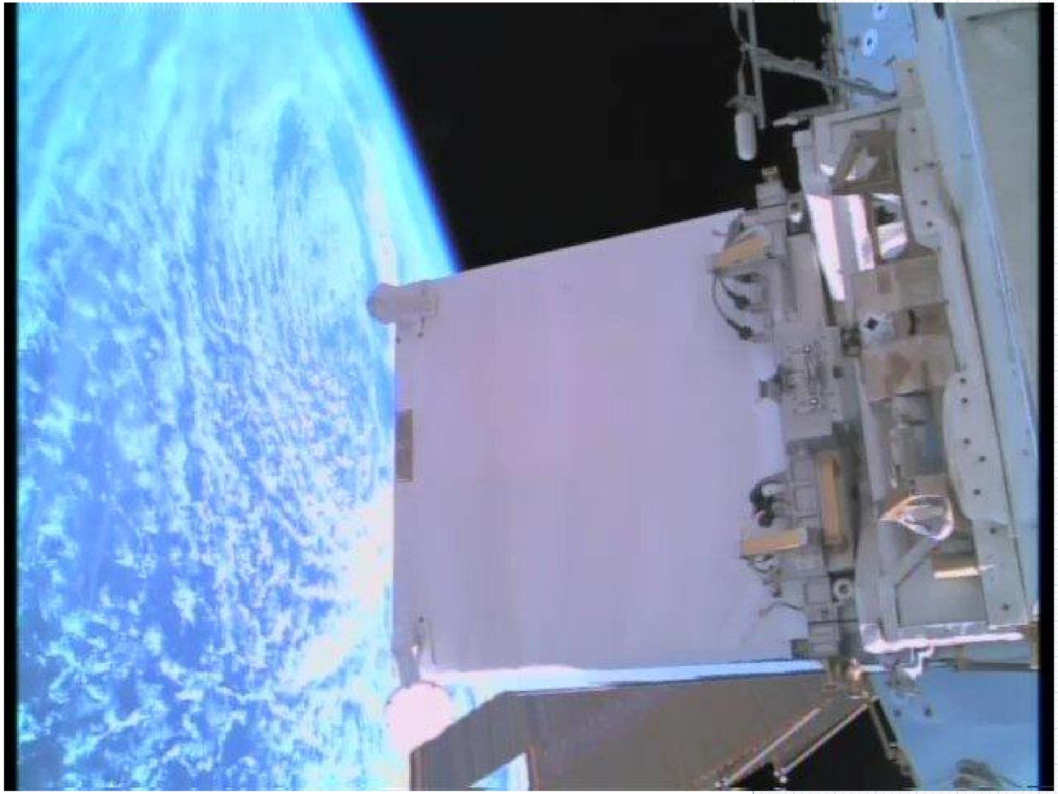

LAGEOS-1, LAGEOS-2 and LARES-2 Pass Statistics (24-Apr-2025 to 7-May-2025)

Station	Location	Average Pass Duration in minutes	Average NPs/Pass	Total Passes
8834	Wettzell	20.5	6.8	129
7090	Yarragadee	19.3	9.4	105
7827	Wettzell (SOSW)	23.9	6.0	85
7841	Potsdam	12.0	6.9	72
7825	Mt Stromlo	18.8	9.7	64
7840	Herstmonceux	29.7	12.2	54
7819	Kunming	2.9	3.2	51
7941	Matera	26.1	12.4	47
7839	Graz	19.4	5.5	34
7810	Zimmerwald	27.5	11.1	33
7845	Grasse	22.6	11.5	32
7237	Changchun	9.7	4.8	27
1884	Riga	15.5	8.1	26
7105	Greenbelt	18.7	9.3	24
7249	Beijing	3.5	3.3	20
7824	San Fernando	20.0	10.5	18
7817	Yebes	15.1	7.9	15
1824	Golosiiv	16.2	6.0	14
7701	Izana	10.7	5.9	14
7821	Shanghai	18.5	8.9	13
7119	Haleakala	27.1	12.8	12
7811	Borowiec	20.5	11.6	11
7306	Wuhan	6.7	4.9	10

- ILRS network statistics of stations getting >=10 LAGEOS class passes in a two-week period. Stations highlighted in green averaged 4 or more LAGEOS class per week
- Four of the Chinese systems (Kunming, Changchun, Beijing and Wuhan) do not appear to follow LAGEOS interleaving/sampling guidance

Thoughts on aiding the determination of SLR measurement bias during POD

British Geological Survey

GRAHAM APPLEBY, BGS HONORARY RESEARCH ASSOCIATE, SGF HERSTMONCEUX

Scope

To focus on the primary geodetic aspects of SLR:

- Major contribution to realisation of the ITRF
  - **Accurate** data absolutely critical in this effort
- Determination of long-wavelength gravity field terms
  - In conjunction with dedicated missions
- Which satellites and best observing strategy:
  - Primarily the LAGEOS, LARES-2 and Etalons

Accuracy

- Intrinsically the SLR technique is capable of 1mm range *accuracy*;
- In practice this is a hard aim, but not impossible
- Key is to detect and mitigate long-term, entrenched systematics, station by station
  - As well as detecting transitory ‘glitches’
- All stations were and are found to have *some* systematic bias *
  - From a few mm to a cm or more from sources:
    - Target-board survey error; ToF hardware error; variable return rates, etc.

* J Geod, 2016

Strategy that was used for ITRF2020

- Great deal of work done by the CCs using AC’s ‘SSEM’ solutions that solve for RB **and** ref frame
  - Average RBs found empirically per station and at variable time intervals;
  - Used to populate data handling file
  - ACs re-run solutions *using* averaged RB
    - i.e., a two-stage process was needed for ITRF2020
    - Mostly, RB is not solved-for during this 2nd stage

Impact on ongoing station practices

- Most important is that any bias remains *fixed* for as long a time period as possible
  - i.e., hardware/practices **not often** ‘tuned’
  - A fixed bias **will be determined** during analysis

- Essential that site logs are modified to follow changes
  - Particularly important in order to inform CoM updates that are system dependent:
    - Rodriguez, 2019, JoG

Impact on ongoing observing practices

- Given the need (mostly) for RB to be solved-for **together with the reference frame**:

- Lots of data!
  - Very useful to get low elevation parts of passes:
  - This greatly helps the maths separation of height & RB:
  - At high elevation, **almost no separation possible** between a station height change and a RB

Thoughts

- It is recommended that:
- Track **LAGEOS & LARES-2** to **as low an elevation as the system normally permits**.
- Resist quitting at low elev. to get another sat!
- Attempt to get returns as early as possible in a pass

Heights of two stations with RB solved each 7-day arc

Height velocity stabilities at 0.1mm/y

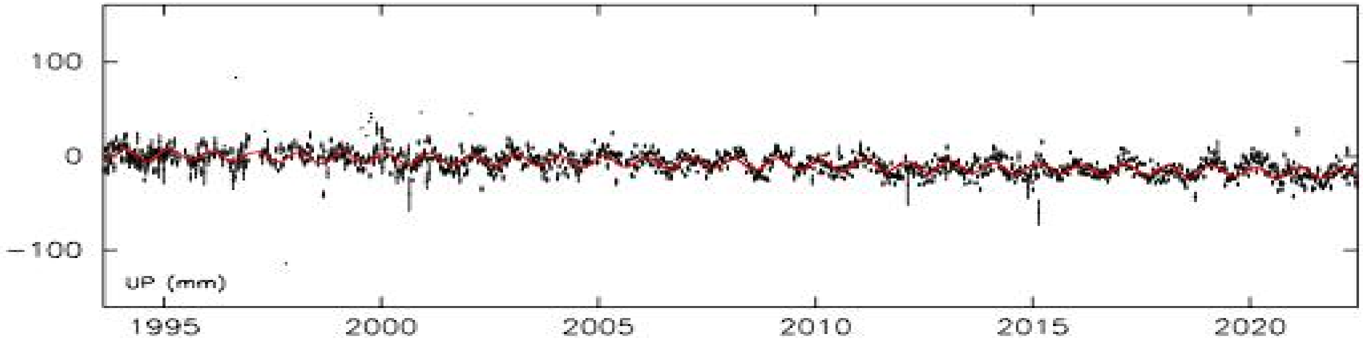

7090

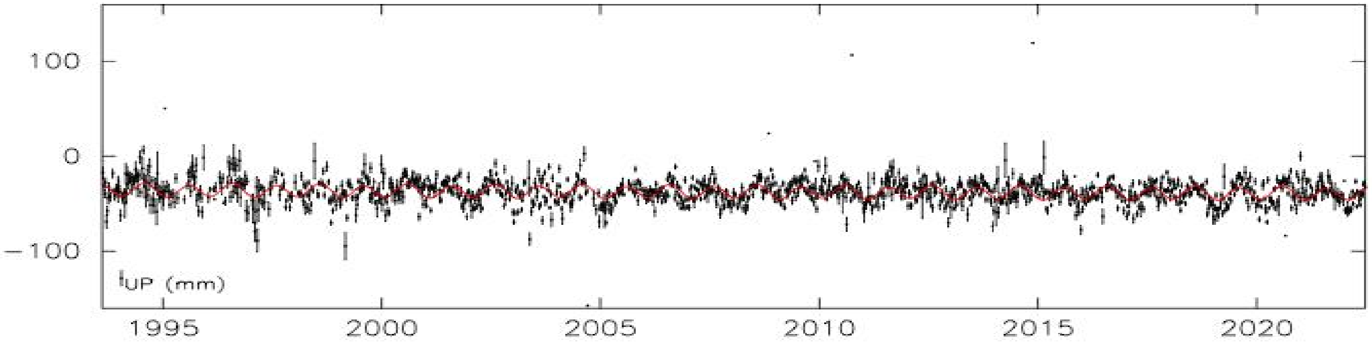

7840

Call for Papers

23RD INTERNATIONAL WORKSHOP ON LASER RANGING (IWLR)

- **NO Conference Proceedings of 23rd-IWLR**
- **All reports downloadable @:**

  https://23rdworkshop.casconf.cn/

  Upload/modify deadline: Aug.31, 2025

- **Special issue by:**

  Astronomical Techniques and Instruments

Astronomical Techniques and Instruments

Call for Papers

Special Issue on Satellite Laser Ranging

Astronomical Techniques and Instruments invites submissions for a Special Issue on " Satellite Laser Ranging (SLR)". SLR is a pivotal technique in high-precision space geodesy and geodynamics, enabling critical applications such as satellite orbit determination, Earth gravity field modeling, and crustal motion monitoring. Recent advancements in laser technology, detector capabilities, and data processing methods have significantly enhanced SLR’s accuracy, data coverage, and scope. This special issue aims to showcase cutting-edge research and foster academic exchanges in this field.

Topics of Interest

(include but are not limited to)

- Design and optimization of SLR systems
- High-precision synchronization and data processing
- Applications in geodynamics, space object monitoring, and orbit determination
- Novel laser sources, detectors, and optical components
- Multimodal integration and future technological perspectives
- Scientific inversions and applications of SLR data

Dr. Ming Li
Sun Yat-sen University

Dr. You Zhao
National Astronomical Observatories, Chinese Academy of Sciences

Submit by **2025.12.31** @ *www.ati.ac.cn*

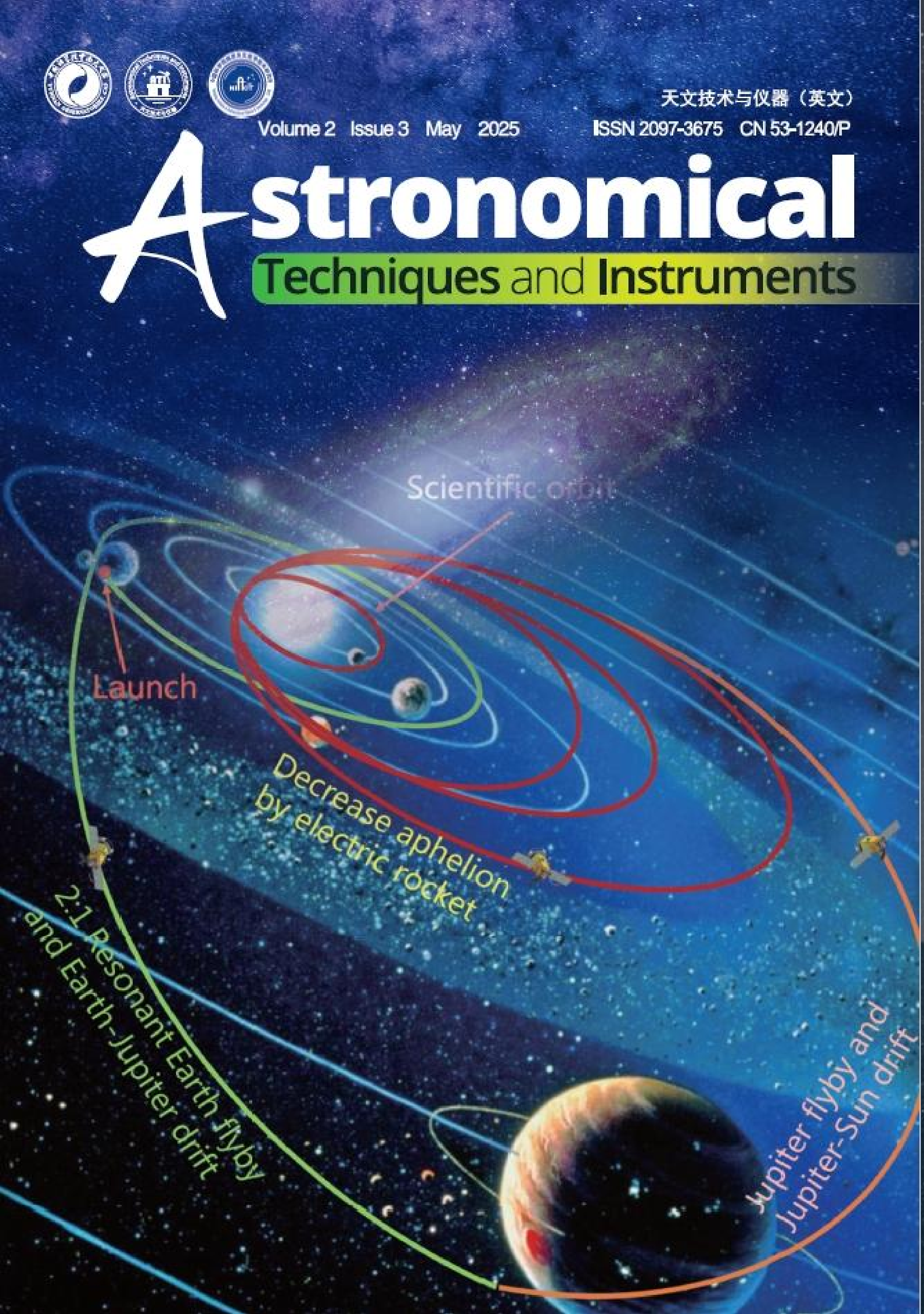

ATI (Astronomical Techniques and Instruments)

- **http://www.ati.ac.cn/**
- Supervised by: Chinese Academy of Sciences
- Sponsored by:

  Yunnan Observatories, CAS

  Nanjing Institute of Astronomical Optics & Technology, CAS
- Bimonthly , Since 1977

About the Special issue

- By now, 2 papers are accepted (previous DL Jun.25)
- Paper collecting time: now ~ December, 2025
- **Submit deadline: Dec.31, 2025**
- By the end of 2025, advertising/summarizing column of SLR topics is to be emphasized.
- Paper collection of the special issue will be released next January.